THESIS FOR THE DEGREE OF DOCTOR OF PHILOSOPHY

Bridging scales in nuclear physics

Microscopic description of clusterization in light nuclei

DANIEL SÄÄF

Department of Physics
CHALMERS UNIVERSITY OF TECHNOLOGY
Göteborg, Sweden 2016

Bridging scales in nuclear physics
Microscopic description of clusterization in light nuclei
DANIEL SÄÄF
ISBN 978-91-7597-408-8

Doktorsavhandlingar vid Chalmers tekniska högskola
Ny serie nr. 4089
ISSN 0346-718X
Department of Physics
Chalmers University of Technology
SE-412 96 Göteborg
Sweden
Telephone: +46 (0)31-772 1000

Cover:
Overlap function of $\left\langle {}^{6}\mathrm{He}(0^+)\right| {}^{4}\mathrm{He}(0^+) + n + n\rangle$ in the $S = L = 0$ channel. The two peaks correspond to the di-neutron and the cigar configurations, respectively, which are characteristic for Borromean two-neutron halo states. The microscopic derivation of the three-body overlap function and results will be presented further in Chap. 5.

Chalmers Reproservice
Göteborg, Sweden 2016

Bridging scales in nuclear physics
Microscopic description of clusterization in light nuclei
Thesis for the degree of Doctor of Philosophy
DANIEL SÄÄF
Department of Physics
Chalmers University of Technology

Abstract

In this thesis we present the ab initio no-core shell model (NCSM) and use this framework to study light atomic nuclei with realistic nucleon-nucleon interactions. In particular, we present results for radii and ground-state energies of systems with up to twelve nucleons. Since the NCSM uses a finite harmonic oscillator basis, we need to apply corrections to compute basis-independent results. The derivation, application, and analysis of such corrections constitute important results that are presented in this thesis. Furthermore, we compute three-body overlap functions from microscopic wave functions obtained in the NCSM in order to study the onset of clusterization in many-body systems. In particular, we study the Borromean two-neutron halo state in ^{6}He by computing the overlap function $< {}^6\mathrm{He}(0^+)|{}^4\mathrm{He}(0^+) + n + n >$. We can thereby demonstrate that the clusterization is driven by the Pauli principle. Finally, we develop state-of-the-art computational tools to efficiently extract one- and two-body transition densities from microscopic wave functions. These quantities are important properties of many-body systems and are keys to compute structural observables. In this work we study the core-swelling effect in ^{6}He by computing the average distance between nucleons.

Keywords: nuclear physics, no-core shell model, halo nuclei, clusterization, transition densities, overlap functions

Acknowledgements

I would like to express my most sincere gratitude to:

Christian Forssén, my supervisor, for patient guidance through the field of physics, for constant support throughout the years and for extraordinarily assistance when finalizing this thesis.

Håkan Johansson, for learning me the things I needed to know, the things I did not knew I needed and the things I do not yet know if I need.

My colleagues for encouragement, companionship, expertise and for coffee breaks with funny stories or complete silence.

The Bergen/Gothenburg physic crew for inspiration and everlasting conversations about life and physics in the Norwegian countryside.

All friends and family for endless patience, interest, care and support through the years.

Hanna, for love and encouragement. I love you.

Finally, I would like to devote a special thought and express my gratitude to my grandmother Dagny and my grandfather Arne for all their love and support.

Thesis

This thesis consists of an extended summary and the following appended papers:

Paper A:
Microscopic description of translationally invariant core + N + N overlap functions
Daniel Sääf and Christian Forssén
Physical Review C 89 (2014) 011303(R)

Paper B:
Infrared length scale and extrapolations for the no-core shell model
Kyle A. Wendt, Christian Forssén, Thomas Papenbrock, Daniel Sääf
Physical Review C 91 (2015) 061301(R)

Paper C:
Pushing the frontier of exact diagonalization for few and many-nucleon systems
Boris D. Carlsson, Daniel Sääf, Håkan T. Johansson and Christian Forssén
In preparation

Paper D:
Transition Densities in the NCSM: Microscopic description of core-swelling in ^{6}He
Daniel Sääf, Håkan T. Johansson and Christian Forssén
In preparation

Contribution report

There are multiple authors of the papers presented and my contribution to each of them are listed below.

A Responsible for the derivation and the implementation of the three-body overlap function. Performed all calculations and created all the figures. Contributed to the writing of the manuscript.

B Responsible for the computation of observables and for testing the derived extrapolation.

C Responsible for the exploratory study of the corrections due to IR and UV cutoffs. Performed all computations and responsible for writing the result section of the manuscript. Contributed to the development of the code with user information and bug reports.

D Responsible for the writing of the manuscript and the code development. Derived and implemented the spin-coupling part of the code and the calculation of nucleon-nucleon distances. Performed all calculations presented in the manuscript.

Contents

Part I
Extended Summary

Chapter 1

Introduction

Nuclear physics has played and is playing an important role in the quest of understanding the building blocks of matter and how they are bound together. It is well known that the Standard Model of particle physics successfully describes the strong interaction between quarks and gluons. However, modelling the atomic nuclei based on its basic constituents and the strong interaction, does not seem to capture the complexity of atomic nuclei. Despite the tremendous efforts put into modelling the hadron-hadron interaction and properties of atomic nuclei using Lattice-QCD, we are still far from a realistic result when computing the masses for even the lightest nuclei in this approach [1].

One reason why this reductionistic approach fails is that the relevant energy scale of nuclear physics does not resolve the dynamics of quarks and gluons. Instead protons, neutrons and pions (the lightest hadrons) emerge as the relevant degrees of freedom. Therefore, an effective field theory (EFT) can be constructed, referred to as chiral EFT, which utilizes a separation of scales in the hadron spectrum while obeying the symmetries of QCD. From chiral EFT realistic nuclear interactions can be obtained and these interactions are used extensively in this thesis. A more detailed description will be presented in Sec. 2.3.

Irrespective of the interaction, the many-body problem of strongly interacting nucleons is a difficult problem to solve. The two-, three- and, in some cases, the four-body problem can be exactly solved. However when the number of degrees of freedom increases the complexity of the problem grows combinatorically. The resulting Schrödinger equation becomes extremely challenging to solve numerically even on powerful supercomputers. There are, however, several many-body methods that can be used to solve the

Schrödinger equation for some of these strongly interacting many-body systems. In this thesis, the No-Core Shell Model (NCSM) will be the method of choice.

A realistic description of atomic nuclei needs to cover a large variety of physics since they exhibit phenomena that span several time and energy scales. Clearly, different many-body structures will emerge in a nuclear landscape that span the lightest isotopes with just a few nucleons to nuclei consisting of hundreds of them. An area in this landscape of isotopes where the different scales are particularly apparent, is where nuclear binding ends. This is called the dripline and nuclei close to the dripline are unstable and quickly decay. The development of radioactive ion beam facilities has been crucial to make it possible to create unstable nuclei and study them even if their lifetimes are short.

1.1 Halo physics

Halo structures are particularly interesting many-body states. They appear close to the dripline and are characterized by unusually large radii [2]. Indeed, it was through extracting the root-mean-square (rms) matter radius from interaction cross-section measurements that Tanihata et al. [3] and Jonson et al. [2] discovered the first known nuclear halo state in ^{11}Li. A halo state is formed when the confining barrier of the nucleons is small, i.e. when their separation energy is small. Furthermore, these nucleons should occupy a low angular momentum state, to reduce the effective angular momentum barrier. Neutron halo systems are more pronounced due to the confining nature of the Coulomb barrier for protons.

The ground states of ^{11}Li and ^{6}He are examples of two-neutron halo nuclei, i.e. where two neutrons are orbiting a core nucleus. A property that makes these particular halo states interesting is that the respective two-cluster subsystems, 2n, ^{5}He and ^{10}Li are unbound. For this reason these systems are sometimes called Borromean halo nuclei [4]. The name originates from the *Borromean rings*, the heraldic symbol of the family of Borromeo, which is a system of three rings connected, in such a way that if one ring is removed the other two rings are disconnected, see Fig. 1.1.

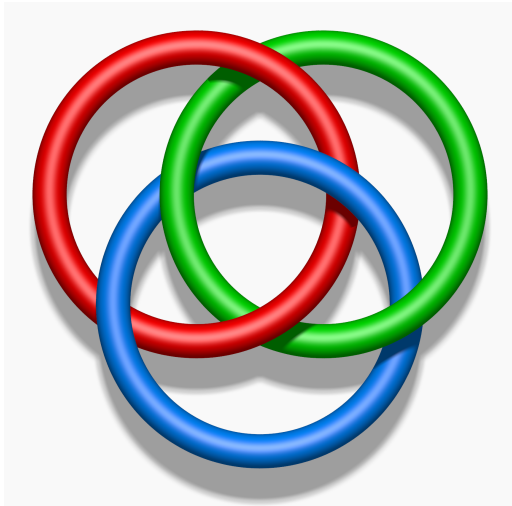

Figure 1.1: *Illustration of the Borromean rings. Figure from Ref. [5]*

1.2 *Ab-initio* methods

Recent developments in theoretical nuclear physics have opened up an avenue for a bottom-up description of the atomic nuclei that is rooted in a microscopic description of the nuclear force. Methods and approaches of this kind are usually called *ab initio* methods after the Latin term for *from the beginning*. The rationale for such an approach to nuclear physics is to be able to control all approximations at each step in the calculations. In turn, this enables performing rigorous uncertainty quantification of computed results. Directly linking the measured observables with *ab initio* results creates an opportunity to make more reliable predictions for observables that are challenging or impossible to measure.

In the last decade there has been a tremendous increase in the number of isotopes that can be accurately described with *ab initio* methods [6, 7]. One of the reasons for this progress the increase of computational power, basically following Moore's law. The *ab initio* approach results in large-scale problems that need powerful computational resources. Consequently, with more resources available, *ab initio* methods can be applied to larger systems. Moreover, we have seen the appearence of new many-body methods with a more gentle scaling with the number of particles [6, 7]. Another reason behind the increasing popularity of *ab initio* methods is the development of realistic nuclear interactions based on chiral EFT.

Ab initio methods are important to understand the mechanism behind the clusterization exhibited by halo nuclei. In particular, it is interesting to study the appearance of new length- and energy-scales from a microscopic perspective. In clusterized states, the number of relevant degrees of freedom can be reduced. Indeed, halo states can be described in terms of a core plus loosely bound valence nucleons. It is the purpose of this thesis to use An *ab initio* theory to bridge the gap between nucleonic degrees of freedom and cluster models and provide insights into the driving force of the clusterization.

This thesis is organized as follows: The NCSM will be presented in more detail in chapter 2. The following chapter 3 deals with the consequences of performing calculations in a finite oscillator basis and how corrections can be applied to extrapolate to results of infinite model spaces. In chapter 4, the method of computing observables with transition densities will be presented and our code ANICRE will be presented. The subsequent chapter 5 introduces a framework to study the clusterization in two-neutron halo systems through overlap functions, and applies it to the halo state of ^{6}He. In chapter 6, a final conclusion of this work is presented together with a brief outlook. Finally, chapter 7 rounds off with a summary of the appended papers.

Chapter 2

No-core shell model

A many-body method needs to be used to be able to solve the A-body Schrödinger equation. In this work, with a focus on the light nuclei and in particular ^{6}He, the NCSM has been the method of choice. In this chapter I will give a brief description of this method and explain why it is suitable for our purposes.

The name NCSM suggests a similarity with the nuclear shell model (SM). The most important difference is that the NCSM does not assume an inert core but treats all particles as active, hence no-core in the name. The idea, however, is similiar; to use the harmonic oscillator (HO) basis and powerful second-quantization techniques. Therefore, the underlying technology is the same as in the SM. However, in the NCSM one uses realistic nucleon-nucleon interactions and aims to solve the full A-body problem without approximations. The interactions used in this work will be introduced in Sec. 2.3.

The specific aim is to solve the A-body Schrödinger equation

$$H_A\psi_A = E_A\psi_A, \tag{2.1}$$

which is the equation governing a non-relativistic quantum system. This goal is achieved by representing the Hamiltonian in a truncated many-body basis and diagonalizing the resulting matrix to get the eigenvalues E_A and corresponding eigenvectors ψ_A. The dimension of the matrix can be huge because the basis grows rapidly with A and many basis states are needed for convergence. A diagonalization method with the capability to handle this kind of problem is the Lanczos method, which is used in most of the present-day NCSM implementations and in all calculations presented in this thesis. The Lanczos algorithm will be presented in more detail in Sec. 2.4.

2.1 Many-body theory and second quantization

A fundamental tool that is used in the NCSM and that is utilized extensively in this thesis is the second quantization formalism. This framework is based on the concepts of Fock space and creation and annihilation operators. A fermionic single-particle (sp) state is denoted $|\alpha\rangle$, where α is a set of quantum numbers needed to describe the state. In second quantization it is possible to write the same state as a fermionic creation operator acting on the vacuum,

$$|\alpha\rangle = a_\alpha^\dagger |0\rangle .$$

We can also introduce an annihilation operator, a_α, which annihilates the state $|\alpha\rangle$. The annihilation operator is the Hermitian conjugate of the creation operator.

The Fermi-Dirac statistic of fermions are ensured by the anticommutation rules for the creation and annihiliation operators. The anticommutation rules for fermions are

$$\{a_\alpha^\dagger, a_\beta^\dagger\} = 0, \qquad \{a_\alpha, a_\beta\} = 0, \qquad \{a_\alpha^\dagger, a_\beta\} = \delta_{\alpha,\beta}. \tag{2.2}$$

In this framework it is now possible to create antisymmetric many-body states, named Slater determinant (SD) states, by acting on the vacuum with multiple creation operators in a given order,

$$|\alpha_1, \ldots \alpha_{A-1}\alpha_A\rangle = a_{\alpha_A}^\dagger a_{\alpha_{A-1}}^\dagger \ldots a_{\alpha_1}^\dagger |0\rangle . \tag{2.3}$$

The basis employed in NCSM computations needs to differentiate between protons and neutrons. This can be achived by using the isospin formalism, which adds two quantum numbers to describe the state: the isospin t and its projection m_t. For nucleons we have $t = \frac{1}{2}$ and $m_t = -\frac{1}{2}$ $(+\frac{1}{2})$ for proton (neutron) states. Many-body theory and second quantization is a broad subject that can be studied in more detail in for example Refs. [8, 9].

2.2 Many-body basis

The many-body basis consists of A-body SD states, as introduced in Sec. 2.1. The most important feature of the SD states is that they are completely antisymmetric with respect to particle exchange. Every SD state is composed of a linear combination of A sp states in sp coordinates. In the NCSM, these

sp states correspond to HO eigenstates. The HO sp states are in coordinate representation defined as:

$$\begin{aligned}\psi_{nljm}(\vec{r},\sigma:b) &= \langle r,\hat{r},\sigma:b|\ nljm\rangle \\ &= R_{nl}(r:b)\left[Y_l(\hat{r})\times\chi_{\frac{1}{2}}\right]^j_m,\end{aligned} \tag{2.4}$$

where the spin, $s=\frac{1}{2}$, is coupled together with the orbital angular momentum l to a total spin j, with a $z-$projection m. R_{nl} is the HO radial function, Y_{lm} is the spherical harmonic function, while $\chi_{\frac{1}{2}}$ is the eigenspinor. Furthermore, b is the HO length and is related to the HO frequency, Ω, via

$$b=\sqrt{\frac{\hbar}{m_N\Omega}}, \tag{2.5}$$

where m_N is the nucleon mass. The HO frequency is a basis parameter that can be varied together with the basis truncation (see below). The quantum number n is the principal quantum number and corresponds to the number of radial nodes of the HO function. The combination $N=2n+l$ corresponds to the eigenenergy of the HO state in the units of $\hbar\Omega$ and is called the major HO shell number.

The HO basis has certain advantages that makes it useful in many-body calculations. First of all, the HO basis states are easy to handle both in momentum and in position space. This makes straightforward to compute matrix elements from interactions expressed both in position and momentum space.

Another advantage is that there are algebraic transformations that simplify the calculations. For example, the Talmi-Moshinsky transformation makes it possible to transform a system of two HO states described with sp coordinates to a system described in relative coordinates [10]. This will be important in the derivation of the overlap functions described in Chap. 5.

Finally, a very prominent advantage of the HO basis is that it is possible to select a truncation such that an A-body state can be factorized into one part dependent only on the center of mass (CM) motion and one part dependent on the intrinsic motion, even if sp coordinates are used. The trick is to truncate the many-body basis by a maximum total HO energy. The physical eigenstate, which is translationally invariant, can then be selected by shifting all spurious CM excitations up in the eigenspectrum using a Lawson projection term [11]. The obtained eigenstates in the SD basis can

then be written as

$$\begin{aligned}&\langle \vec{r}_1 \dots \vec{r}_A \sigma_1 \dots \sigma_A \tau_1 \dots \tau_A |\, AJM \rangle_{SD} \\ &= \left\langle \vec{\xi}_1 \dots \vec{\xi}_A \sigma_1 \dots \sigma_A \tau_1 \dots \tau_A \right|\, AJM \Big\rangle \, \Psi_{000}(\vec{\xi}_0),\end{aligned} \tag{2.6}$$

where ξ_i are relative Jacobi coordinates, which will be introduced in more detail in Chap. 5. The ξ_0 corresponds to the center of mass coordinate and the CM motion is in the $0S$ ground state. One drawback of the harmonic oscillator basis is the rapid Gaussian falloff ($\backsim e^{-\alpha r^2}$) of the basis functions at large r. This is much steeper than the expected asymptotic behaviour of atomic nuclei, which is $\backsim e^{-\beta r}$, where β is related to the single-nucleon separation energy. This mismatch makes it difficult to describe the asymptotic behaviour correctly in the NCSM, in particular for halo nuclei, that have small separation energies.

In principle, a complete, i.e. infinite, many-body basis will assure that the Schrödinger equation is solved exactly. In practice, however, the basis needs to be truncated. The truncation scheme that we use is, as indicated above, based on the total energy of the many-body state. The total energy of a SD state is the sum of the energies of the A HO states,

$$E_{\text{tot}} = \sum_{i=1}^{A} N_i \hbar\Omega = \sum_{i=1}^{A} (2n_i + l_i)\hbar\Omega = N_{\text{tot}}\hbar\Omega.$$

Instead of labelling a many-body truncation by $\sum_i N_i \leq N_{\text{tot}}$ we rather introduce the parameter $N_{\max}$, which measures the maximal allowed number of HO excitations above the lowest possible configuration, N_0. N_0 is defined as $N_0 = \sum_i^A N_i$ without excitations, as shown in Fig. 2.1. For s-shell nuclei we have $N_0 = 0$ and therefore $N_{\max} = N_{\text{tot}}$. For p-shell nuclei it will depend on how many particles are in the $N = 1$ shell in the lowest configuration. For example, in ^{6}Li we have $N_0 = 2$ and consequently $N_{\max} = N_{\text{tot}} - 2$. In Fig. 2.1 we illustrate four different configurations of ^{6}Li. All $N_{\text{tot}}\hbar\Omega$ configurations with $N_{\text{tot}} = \sum_i N_i \leq N_{\max} - N_0$ where $N_{\max}$is even (odd) for natural (unnatural) parity span the $N_{max}\hbar\Omega$-space.

There is a choice in how to treat the spin of the many-body states. Either the sp states are spin-coupled to a total J, which then is a good quantum number of the basis. This is called the J-scheme. The other option is that the sp states remain uncoupled, with the total $M_J = \sum_{i=1}^{A} m_i$ becoming the good quantum number. We are using this scheme, which is called the M-scheme. In addition, parity π and M_T are also good quantum numbers. In

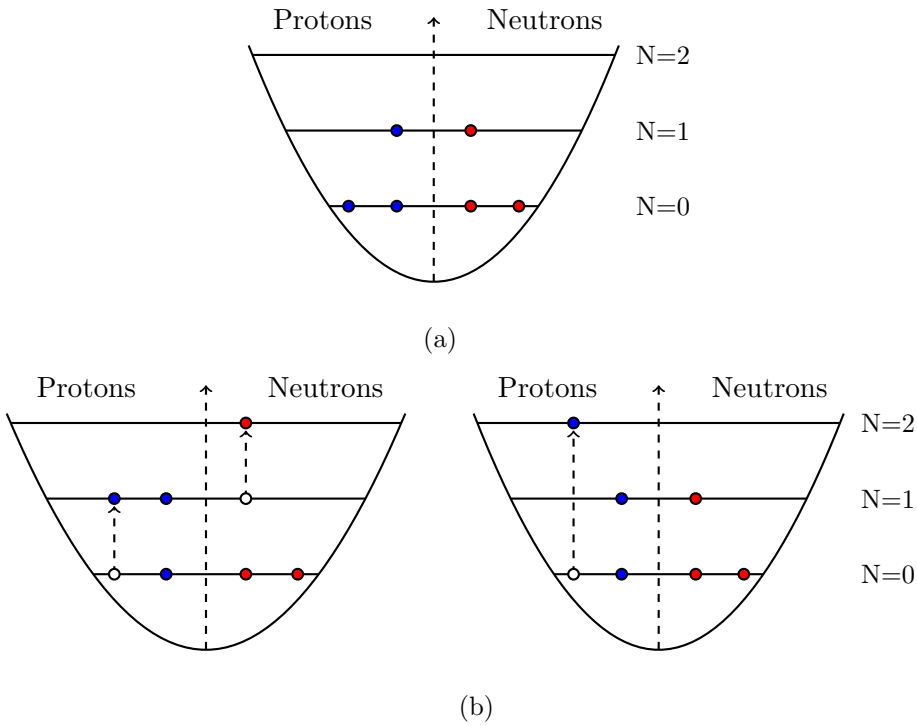

Figure 2.1: *Sketch of many-body states in* ^{6}*Li. Panel a:* $N_{\max} = 0$ *configuration. Panel b:* $N_{\max} = 2$ *configurations.*

an M-scheme basis with a particular M_J, all eigenstates with $J \geq M_J$ can be captured. The advantage of the M-scheme is that the antisymmetrization is trivially achieved and there is no need to include spin-coupling algebra. The disadvantage is that the many-body basis becomes much larger compared with the J-scheme. The M-scheme is more efficient for systems with more than four nucleons and it is therefore used in most NCSM calculations.

2.3 Realistic nuclear interactions

A specific goal of *ab initio* nuclear structure calculations is to employ and test realistic nuclear interactions. Our fundamental understanding of nuclear systems should in principle be based on QCD, which is the theory explaining the strong interaction between quarks and gluons. Nuclear structure, however, is a low-energy phenomenon on the scale of subatomic physics. Since QCD is non-perturbative in this low-energy regime it is very difficult to use it

in direct computations. One way of overcoming this issue is to introduce the concept of an effective field theory (EFT). The crucial starting point for an EFT is to identify a separation of scales. In the case of low-energy nuclear physics a natural separation of scales is observed in the meson spectrum with $m_\pi \ll m_\rho$. The appropriate degrees of freedom are therefore nucleons and pions. Based on this it is now possible to write down a general Lagrangian with nucleon and pion fields obeying the underlying theory, QCD. The Feynman diagrams that result from this Lagrangian can be ordered in powers of Q/Λ_χ, with Q being the momentum scale of the process and $\Lambda_\chi \approx m_\rho$ the breakdown scale of the EFT. Consequently, the leading order (LO) is the most important one. The EFT contain loop diagrams that need to be renormalized and therefore a chiral regulator (characterized by a cutoff scale Λ_{EFT}) is needed.

The effect of using a low-energy EFT is that all short-range physics is condensed into contact terms in the Feynman diagrams. The strength of these contact terms can be determined by fitting model predictions to experimental nucleon-nucleon scattering data. In this work two different nucleon-nucleon (NN) potentials based on chiral EFT have been used. The first one was developed by Entem and Machleidt [12] and contains diagrams up to next-to-next-to-next-to leading order (N3LO). This potential will further on be referred to as Idaho-N3LO (I-N3LO). The other one, NNLOopt, was developed by Ekström et al. [13] including diagrams up to NNLO. The low-energy constants in the NNLOopt potential was determined by using POUNDERS [14], a modern mathematical optimization algorithm. Both NNLOopt and I-N3LO use a non-local chiral regulator with $\Lambda_{EFT} = 500$ MeV.

2.3.1 Three-body forces

For a complete description of nuclear forces it is not enough with a NN interaction. A realistic interaction-model needs to include also irreducible many-body forces. In the chiral EFT power counting the three-body force diagrams enter at next-to-next-to-leading order (NNLO) and seem to play an important role in reproducing the physics of atomic nuclei. In this work we have mainly considered two-body forces because it gives us the opportunity to solve the eigenvalue problem in really large model spaces. However, the frameworks presented in Chap. 5 and Chap. 4 are not restricted to any specific type of interaction.

2.3.2 Unitary transformations

Realistic nucleon-nucleon potentials are characterized by a hard core (short-range repulsion) and a strong tensor force. The result of this is that low-energy physics is still dependent on higher momentum modes, and that very large model spaces are required to capture all relevant UV physics. There are different solutions to this problem, but a particularly useful one is to apply a unitary transformation that uncouples the low- and high-momentum modes from each other while keeping the physical observables unchanged. This procedure can be viewed as lowering the resolution scale of the problem to one that is more suitable for a truncated basis. The transformation needs to be unitary to keep the observables, such as the energy, invariant. The unitary transformation used in this work is the similarity renormalization group (SRG) [15].

The SRG transformation is implemented as a flow equation and uses a diagonal flow-generator to suppress the off-diagonal matrix elements in momentum space. The transformation therefore evolves the potential towards a band-diagonal form and decouples the high-momentum modes. There is a flow parameter, Λ_{SRG}, which is defined such that $\Lambda_{\mathrm{SRG}} = \infty$ means no transformation and $\Lambda_{\mathrm{SRG}} = 0$ corresponds to taking the flow to infinity. In principle, the SRG flow induces many-body forces. The calculations performed in the scope of this work will only take into account effective two-body forces. This approximation violates the unitarity of the transformation and creates a dependence on the SRG flow parameter. The magnitude of this dependence can be seen as an indicator of missing induced many-body forces. However, it is important to note that the technical developments presented in Paper C, allow us to perform the calculations in larger model spaces. Consequently, most of the calculations presented in this thesis are performed with bare interactions, i.e. not evolved.

2.4 Matrix diagonalization and computational challenges

In the NCSM the many-body problem is translated to an a eigenvalue problem. This is achieved by expressing the wave function in a many-body basis, $|\Psi_A\rangle = \sum_i c_i |\sigma_i\rangle$, where $|\sigma_i\rangle$ are many-body basis states and c_i are unknown (variational) parameters that need to be determined. Eq. (2.1) can

now be written as

$$\sum_{i=1}^{D} \langle \sigma_j | \, H \, | \sigma_i \rangle \, c_i = E c_j.$$

This generates an eigenvalue problem with $H_{ij} \equiv \langle \sigma_j | \, H \, | \sigma_i \rangle$ being a huge and (somewhat) sparse matrix. For example, ^{6}Li can be computed in a $N_{\max} = 22$ model space, which corresponds to a many-body basis dimension of $D = 2.5 \times 10^{10}$, where the number of non-zero elements is $N_{\text{non-zero}} = 5 \times 10^{14}$. Storing all non-zero matrix elements would correspond to ≈ 6 PB of data. The growth of the basis size with $N_{\max}$ is demonstrated in Fig. 2.2 for a set of isotopes. In addition, the number of non-zero matrix elements in the Hamiltonian is also displayed.

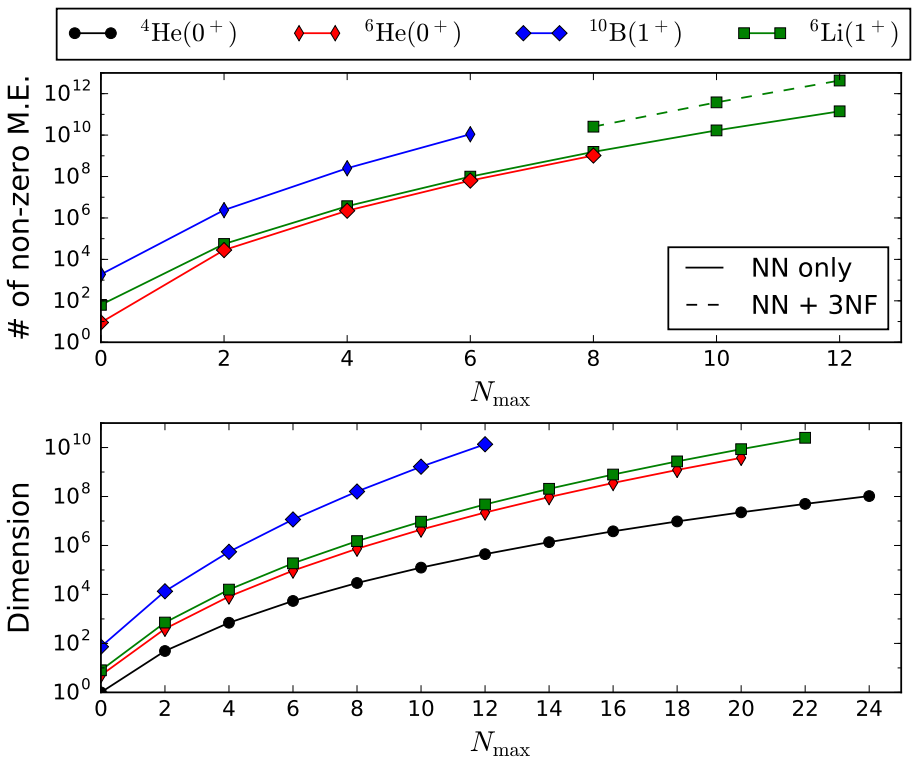

Figure 2.2: *The upper panel shows the number of non-zero matrix elements in the Hamiltonian as a function of* $N_{\max}$*. The lower panel shows the dimensionality of the many-body basis as a function of* $N_{\max}$*.*

The eigenvalue problem can be solved by utilizing the Lanczos algorithm,

which is an iterative methods that yields the extreme eigenvalues first [16, 17]. This is suitable for nuclear structure calculations, since the states of interest are usually the low-energy states. The Lanczos method is very efficient. The most time-consuming step is a matrix-vector multiplication, followed by vector orthogonalization, with the consequence that the CPU time scales like $\mathcal{O}(D^2)$, where D is the dimension of the many-body basis.This can be compared to standard (full) diagonalisation methods that scale like $\mathcal{O}(D^3)$. In addition, the Lanczos algorithm is memory efficient and highly parallelizable.

The idea behind the Lanczos algorithm is to iteratively build up a basis in which the Hamiltonian, H, is tridiagonal and can be written as

$$T_k = \begin{pmatrix} \alpha_1 & \beta_2 & 0 & 0 & \dots & 0 & 0 \\ \beta_2 & \alpha_2 & \beta_3 & 0 & \dots & 0 & 0 \\ 0 & \beta_3 & \alpha_3 & \beta_4 & \dots & 0 & 0 \\ \vdots & \vdots & \vdots & \vdots & \vdots & \vdots & \vdots \\ 0 & 0 & 0 & 0 & \dots & \alpha_{k-1} & \beta_k \\ 0 & 0 & 0 & 0 & \dots & \beta_k & \alpha_k, \end{pmatrix} \tag{2.7}$$

after k iterations. The eigenstates of the small tri-diagonal matrix, T_k are easily computed and correspond to the full spectrum of eigenvalues of H, as $k \to \infty$. However, only a few iterations are needed to converge the lowest-lying eigenvalues. The eigenvectors of the tridiagonal matrix can easily be transformed to the many-body basis. In this way the wave functions are obtained.

The matrix T_k is computed and expanded iteratively. One starts with a normalized basis (pivot) vector $|q_1\rangle$ and that gives the first diagonal value, $\alpha_1 = \langle q_1 | H | q_1 \rangle$. The second basis vector, which needs to be orthogonal to q_1 can now be computed, $|\tilde{q_2}\rangle = H|q_1\rangle - \alpha_1 |q_1\rangle$. The norm of $|\tilde{q_2}\rangle$ is the non-diagonal value, β_1, which normalizes $|q_2\rangle$. $|q_2\rangle$ is now the second vector in the basis. To highlight the expensive matrix vector multiplication we will

introduce an intermediate vector $\left|\tilde{\tilde{q}}_{k+1}\right\rangle = H\left|q_k\right\rangle$. Continuing, we have:

$$\left|\tilde{\tilde{q}}_{k+1}\right\rangle = H\left|q_k\right\rangle \tag{2.8a}$$

$$\alpha_k = \left\langle q_k\right| \left|\tilde{\tilde{q}}_{k+1}\right\rangle \tag{2.8b}$$

$$\left|\tilde{q}_{k+1}\right\rangle = \left|\tilde{\tilde{q}}_{k+1}\right\rangle - \beta_k\left|q_{k-1}\right\rangle - \alpha_k\left|q_k\right\rangle \tag{2.8c}$$

$$\beta_{k+1} = \sqrt{\left\langle \tilde{q}_{k+1}\right| \left.\tilde{q}_{k+1}\right\rangle} \tag{2.8d}$$

$$\left|q_{k+1}\right\rangle = \frac{\left|\tilde{q}_{k+1}\right\rangle}{\beta_{k+1}} \tag{2.8e}$$

In this recipe, it is clear that the costly step is the matrix vector multiplication, $H\left|q_k\right\rangle$, as all other steps only involve vector operations.

In numerical implementations with finite precision arithmetic, the Lanczos vectors need to be re-orthogonalized to the preceding vectors. This is due to the loss of orthogonality that is introduced as an effect of round-off errors. The origin of the loss of orthogonality can be explained in the following way: When calculating $\left|q_{j+1}\right\rangle$, round-off errors introduces components non-orthogonal to the preceding vectors, which by construction should be orthogonal to $\left|q_{j+1}\right\rangle$. In the next step, when $\left|q_{j+2}\right\rangle$ is computed from $\left|q_j\right\rangle$ and $\left|q_{j+1}\right\rangle$, it will not be orthogonal to $\left|q_1\right\rangle \ldots \left|q_{j-1}\right\rangle$. In this way the error builds up quickly and needs to be handled. There are different ways of handling the re-orthogonalization. A more detailed review of the Lanczos algorithm can be found in Refs. [16, 17].

When performing Lanczos diagonalization, a maximum number of iterations or a convergence criterion needs to be set. To prevent running unnecessary iterations the latter option is generally used. The choice of an accurate criterion is non-trivial since it is dependent on the observable being computed. In ANTOINE, which is the code used in this work, the measure of convergence is how much the converged energy eigenvalues of the computed states changed during the last three Lanczos iterations.

To demonstrate the impact of the choice of the convergence criterion, three different measures of convergence are presented in Fig. 2.3 for a ^{6}Li calculation in a $N_{\max} = 14$ model space. The energy convergence measure is defined to be $\Delta(E_i) = \left|\frac{E_i - E_{i-1}}{E_i}\right|$ at iteration i. In the same manner, the convergence of the radius is defined as $\Delta(r_i) = \left|\frac{r_i - r_{i-1}}{r_i}\right|$ at iteration i. The third definition estimates the changes in the Ritz vector for each iteration. The Ritz vector, is the eigenvector of matrix T_k and its dimension obviously grows for every iteration. The Ritz convergence measure is in this case

defined as $\sqrt{1 - \vec{v}_i \cdot \vec{v}_{i-1}}$, where $\vec{v}_{i-1}$ is zero padded in the components that were added to $\vec{v}_i$. In this way, it is possible to estimate the size of the changes introduced to the wave function by adding another Krylov vector.

The performance of the Lanczos algorithm is demonstrated in Fig. 2.3. It is evident that it takes a number of iterations to capture the physics of the wave function. Additionally, it is important to note that the radius is converging slower than the energy. Therefore, using an energy convergence criterion can give a too optimistic estimate of the convergence of the radius. The change of the Ritz vector seems to be a too conservative measurement of the convergence. One of the goals of *ab initio* methods is to be able to do an accurate error analysis. To achieve that we need to take the errors from the many-body method into account and the use of different convergence criteria needs to be studied further.

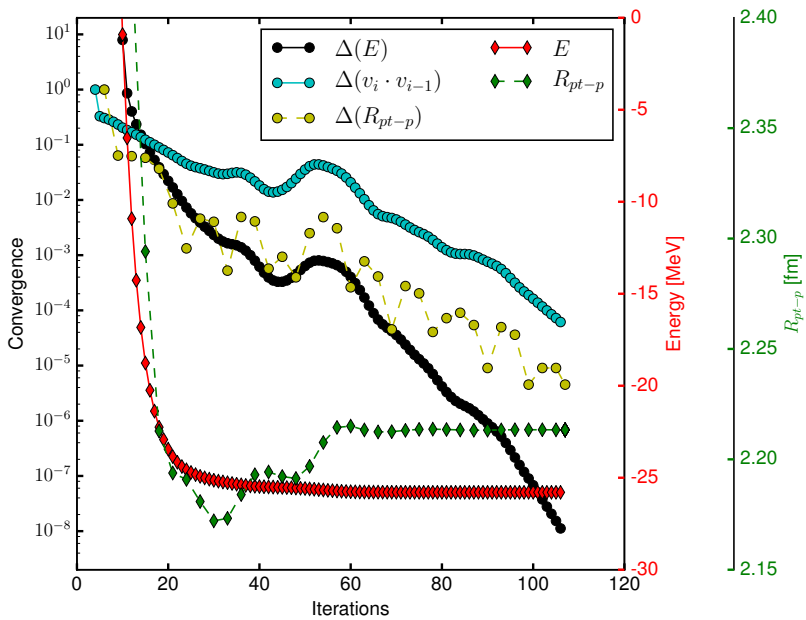

Figure 2.3: *Evolution of different convergence measures. The computed observable for every Lanczos iteration is presented (diamonds) together with the change from previous iteration (circles). The data is collected from a computation of the lowest state of* ^{6}*Li with NNLOopt[13],* $N_{\max}$*=14 and* $\hbar\Omega = 20$ *MeV, starting with a random pivot vector.*

Chapter 3

Correction due to the finite harmonic oscillator basis

Due to the fact that the NCSM calculations utilize a finite harmonic oscillator basis the computed results will be dependent on the model space. As the model space size increases the calculated quantities converge to model-space independent results. However, as described in Chap. 2, the basis size in the NCSM grows rapidly with both A and $N_{\max}$, and therefore, in most of the calculations the results are not fully converged. Consequently, we need to handle the systematic error that arises from the model space dependence.

In recent years, a lot of progress has been made in quantifying the model space dependence in finite oscillator spaces and a framework to systematically compute converged results with a statistical error analysis has been developed [18, 19]. In this chapter, we will introduce the main ideas of this framework and highlight our contributions to it. In particular, we will present how it is applied in the NCSM, based on the research presented in Paper B. The last part of this chapter will focus on the extrapolation of energy eigenvalues and in particular the exploratory study presented in Paper C. This development is important in the quest of controlling all approximations and constitutes a useful tool to quantify errors that originate from the truncated HO basis, as well as a means to provide meaningful values even when fully converged calculations are not feasible.

3.1 Infrared and ultraviolet cutoff

The model space in NCSM are characterized by the HO frequency, $\hbar\Omega$, and the total number of included HO excitations above the lowest configuration, $N_{\max}$. In Fig. 3.1 results for the ground-state energy of ^{4}He are presented as a function of $\hbar\Omega$, for different model space sizes. The dependence on the

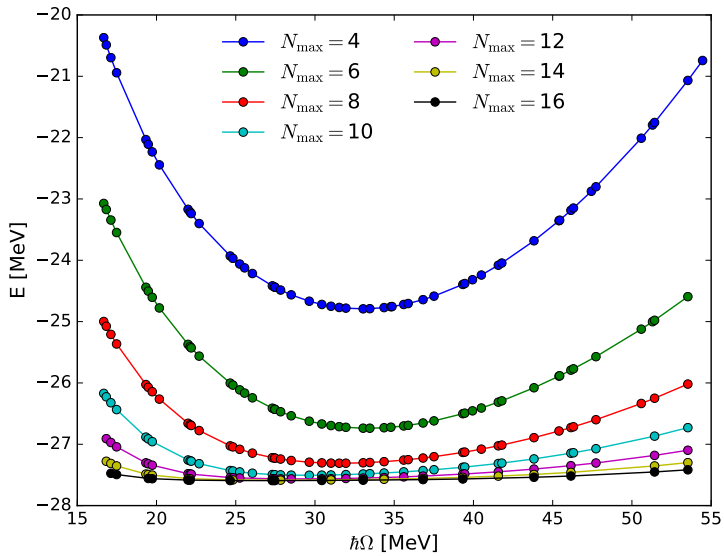

Figure 3.1: *Ground-state energy of ^{4}He as a function of $\hbar\Omega$. Computed with* ANTOINE*, using the NNLOopt interaction [13].*

model-space parameters is clearly visible, although the dependence on $\hbar\Omega$ decreases when $N_{\max}$ increases. This effect is manifested by the fact that the lines at constant $N_{\max}$ flatten with higher $N_{\max}$. In addition, the energy is converging from above when the model-space size is increasing, due to the variational principle. The results in Fig. 3.1 include $N_{\max} = 16$. This model space is large enough to obtain converged results in ^{4}He with the bare NNLOopt interaction. However, when studying heavier systems reaching convergence is not always feasible, which is exemplified in Fig. 3.2 where the ground-state energy of ^{10}B is shown as a function of $\hbar\Omega$. In contrast to Fig. 3.1 the results are far from converged and would need to be extrapolated to reach a basis independent result. Note that $N_{\max} = 12$ is the largest model space in which ^{10}B has been computed.

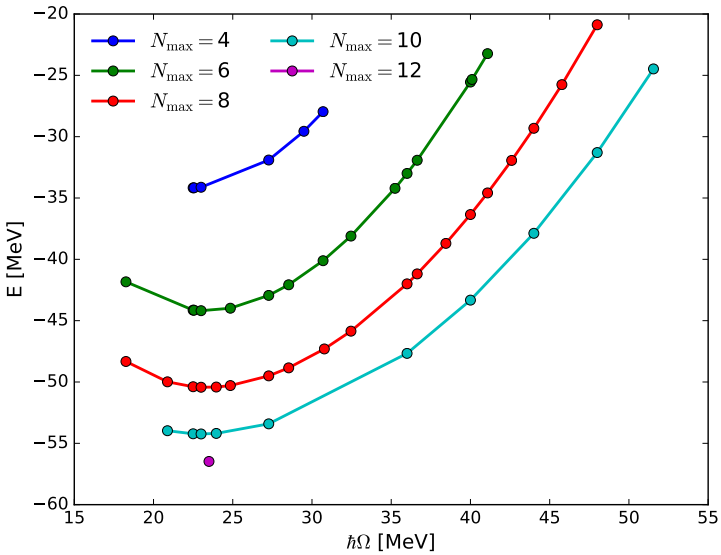

Figure 3.2: *Ground-state energy of* $^{10}B(3^+)$ *as a function of* $\hbar\Omega$*. Computed with* ANTOINE*, using the NNLOopt interaction [13]*

There have been different approaches to extrapolate the finite-space results. The first attempts were based on a phenomenological extrapolation using the $N_{\max}$ and $\hbar\Omega$ parameters [20, 21]. However, in recent years a new approach has been suggested [19, 18]. This approach is based on the fact that the parameters of the HO basis, $N_{\max}$ and $\hbar\Omega$ correspond to an ultraviolet (UV) energy cutoff, and an infrared (IR) length cutoff. This can be motivated by considering a decrease in the HO frequency for a certain $N_{\max}$ model space, which will cause a lower high-energy resolution but a better resolution in the long-range part of the wave function. In Fig. 3.3 this is demonstrated by a set of HO functions, where it is clearly seen that when the HO frequency decreases the spatial extension of the basis states grow. The same effect is caused by an increase in $N_{\max}$. In this way, the HO basis truncation can be viewed as a Dirichlet boundary condition on the wave function, which is dependent on $N_{\max}$ and $\hbar\Omega$. In addition, the same argument can be used in momentum space. Thus, the maximum momentum included in a finite HO basis corresponds to a boundary condition in momentum space at λ_{UV}.

Interactions based on EFT, introduced in Sec. 2.3, have an intrinsic UV cutoff, Λ_{EFT}, as an effect of the renormalization [19]. Typically, for

most available chiral interactions, Λ_{EFT} is around 500 MeV. For data points well above Λ_{EFT} the dependence on Λ_{UV} decreases and by only including computations that are converged in Λ_{UV} we can assume that the data points capture all UV physics included in the interaction. Hence, only the IR dependence needs to be extrapolated. This simplified pictured will be discussed further in Sec. 3.3.

The precise determination of the UV and IR cutoffs for a particular HO space truncation has been the subject of many studies. The first attempt to determine the IR and UV cutoffs was based on the maximum momentum and maximum displacement in the HO basis [22, 23]. For a single-particle HO basis with the harmonic oscillator length b and the total energy $E = \hbar\Omega(N_{\mathrm{tot}} + \frac{3}{2})$, the IR cutoff is to a first approximation

$$L_0 = \sqrt{2\left(N_{\mathrm{tot}} + \frac{3}{2}\right)}b,$$

and the UV cutoff is

$$\Lambda_{\mathrm{UV},0} = \sqrt{2\left(N_{\mathrm{tot}} + \frac{3}{2}\right)}\hbar/b.$$

The IR cutoff corresponds to the classical turning point in the harmonic oscillator potential [23].

Furnstahl et al. [24] later suggested an improvement of the IR scale, based on both empirical studies of sp states in the HO basis and an analytical derivation where they compared the eigenvalues of the p^2 operator in the HO basis with the eigenvalues of the p^2 operator in a finite box with a Dirichlet boundary condition. By equating the lowest eigenvalues of these two spectra the box radius, which corresponds to the IR length scale, could be determined. In the following text, the corresponding cutoffs are labeled L_2 and Λ_2.

3.2 Length scale of the NCSM basis

The naive estimate of the IR and UV cutoff presented in the previous section fail to produce the expected results for many-body systems in the NCSM truncation. This is exemplified in the left panel of Fig. 3.4, where the data with the highest UV cutoff is not lowest in energy at a given L_2. However, the expectation is that data points that are converged in UV only should be

dependent on the IR cutoff. For this reason, an envelope should have been formed by the high UV-data. To solve this issue an accurate IR scale needs to be derived for the NCSM many-body basis.

In Paper B, the scales of the NCSM basis were investigated. Inspired by previous work [25], the aim was to equate eigenvalue of the kinetic energy operator in the NCSM basis to the eigenspectrum of the kinetic operator of a corresponding system in a infinite well of radius L. Consequently, the radius of the well corresponds to the Dirichlet boundary of the NCSM basis. Finding the corresponding system was one of the challenges. We realized that a system consisting of A particles in 3 dimensions in a NCSM basis with the energy truncation, N_{tot}, corresponds to a sp state in a 3A-dimensional HO basis, with an energy truncation at N_{tot}, which at low momenta is equivalent to a hyper-radial infinite well. The NCSM eigenstate, in sp coordinates, are a product of a center-of-mass state and an intrinsic state. Thus, the relevant IR length is an intrinsic scale. The intrinsic basis is $3(A-1)$-dimensional. Consequently, the corresponding system is a $D = 3(A-1)$ dimensional hyper-radial infinite well.

By comparing the kinetic energy spectra, demonstrated in Fig. 3.5 we could confirm that the two systems does correspond to each other and we could derive a relation for the IR scale of the NCSM basis:

$$L_{\text{eff}} = b\widetilde{N}(A, N_{\max}, \pi),$$

where b is the HO length and $\widetilde{N}(A, N_{\max}, \pi)$ depends on the model space truncation and the number of particles. It can be obtained by finding the kinetic energy spectrum in a hyper-radial well and in the NCSM basis. However, it is not necessary to compute the kinetic operator in the full dimension of the NCSM basis. More details can be found in Paper B.

In Ref. [26] König et al. investigated the UV cutoff. By exploiting the HO duality between momentum and coordinate space, they determined that similarly to the description of the IR cutoff as a Dirichlet in coordinate space, the UV cutoff can be viewed as a Dirichlet boundary condition in momentum space. Consequently, they derived a relation between L_{eff} and Λ_{eff}. Based on that, the UV cutoff in the NCSM basis is $\Lambda_{\text{eff}} = b^{-1}\widetilde{N}(A, N_{\max}, \pi)$.

In the right panel of Fig. 3.4 the effective NCSM scales are used. In contrast to the left panel, the envelope is formed by the data points with highest Λ_{UV}, as expected.

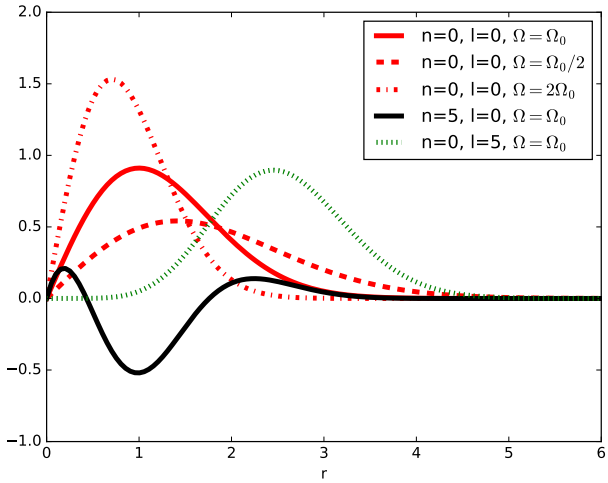

Figure 3.3: *Harmonic oscillator functions plotted for a set of quantum numbers to illustrate that a HO truncation can be viewed as a Dirichlet boundary condition, i.e. spatial confinement.*

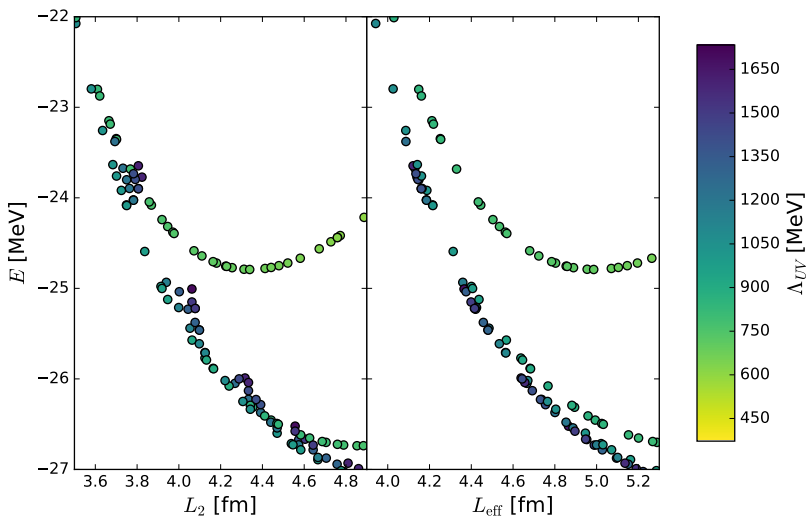

Figure 3.4: *Ground-state energy of* ^{6}*Li computed with the NNLOopt interaction [13] for different definitions of the IR and UV scale. Left panel: The scales obtained in the two-body system,* L_2 *and* $\Lambda_{\mathrm{UV},2}$*. Right Panel: The scales obtained in the NCSM model space,* L_{eff} *and* Λ_{eff}*.*

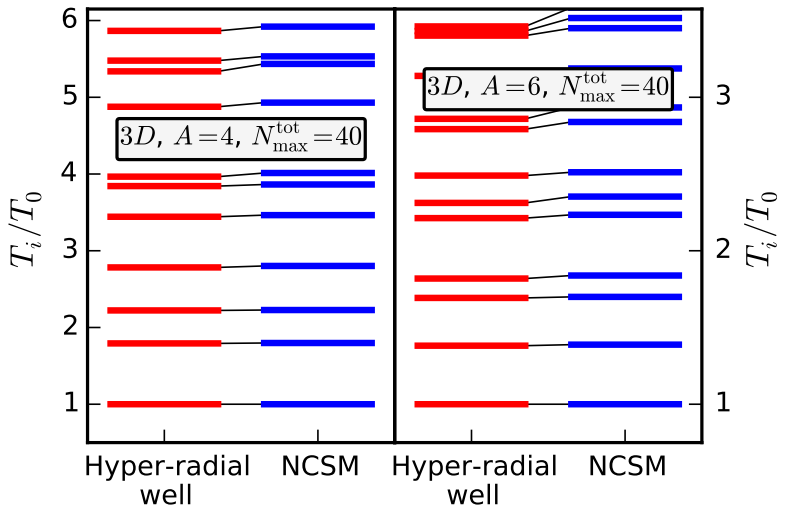

Figure 3.5: *The intrinsic kinetic energy spectra for A=4,6 particles in the NCSM and for the corresponding D=3(A-1) dimensional hyper-radial infinite well.*

3.3 Corrections to observables

After the IR and UV cutoff of the NCSM basis are determined, expressions for the IR corrections need to be derived. As already stated, the UV correction will be assumed negligible when limiting the dataset to only include UV converged data points, where $\Lambda_{\text{UV}} \gg \Lambda_{\text{EFT}}$. In Fig. 3.6 the relation between Λ_{UV} and L_{eff} is illustrated as a function of $N_{\max}$ and $\hbar\Omega$.

The IR correction to the energy was derived by Furnstahl et al. [18]. The derivation was based on results from quantum chemistry, where the effect of putting a hydrogen atom in a spherical infinite well has been determined [27]. They arrived at an expression for the leading-order (LO) IR correction,

$$E(L) = E_\infty + A_0 e^{-2k_\infty L} + \mathcal{O}(e^{-4k_\infty L}), \tag{3.1}$$

where k_∞ is related to the single-nucleon separation energy. However, in the many-body systems E_∞, A_0 and k_∞ will be treated as fitting parameters. To simplify the notation the LO correction term will be labeled: $E_{\text{LO}}^{\text{corr}}(L) = A_0 e^{-2k_\infty L}$. This notation will be used later as more terms are introduced.

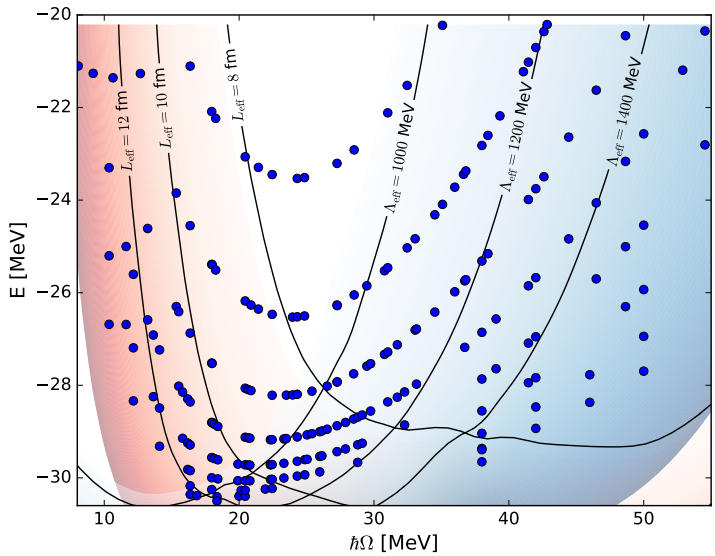

Figure 3.6: ^{6}*Li data computed with NNLOopt [13] as a function of* $\hbar\Omega$*. In addition, the corresponding IR and UV scales are are shown, to illustrate regions with high* Λ_{eff} *and high* L_{eff}*, respectively.*

3.4 Fitting procedure and error estimation

From the data points obtained in a finite HO basis, a basis-independent result can now be extracted by fitting to Eq (3.1). The least-squares method is used to perform the fits, implemented in LMFIT [28]. From the fitting procedure a statistical error on the fitted parameters can be extracted. This error is only due to the least-square fit and does not reflect systematic uncertainties such as missing correction terms.

In Paper C, the bootstrap method was also investigated as a tool to understand the sensitivity of the fit on individual data points. The bootstrap idea is based on the assumption that the original sample represents the underlying distribution, usually named the population. Hence, the original sample can be used to estimate the statistics of the population, which in the bootstrap method is achieved by resampling. New samples are drawn from the original sample with replacement, which implies that a data point in the original sample can occur multiple of times in a new sample. In this way the data points are weighted stochastically. The new samples are constructed to have the same length as the original sample. In our case, a bootstrap distribution is computed from repeated fits to the new sample and statistical properties are extracted from this distribution. A more detailed introduction to the bootstrap method can be found in Ref. [29]. In our case, the computed dataset works as the original sample and a fit is performed on every new sample. In particular this procedure will measure the sensitivity of the fit on individual data points.

In Fig. 3.7 the bootstrap distribution, i.e. the distribution of extrapolated E_∞ from the bootstrap samples, is shown for different number of resamples from a set of ^{6}Li results. It is clear that the distribution converges to a normal distribution. From the bootstrap distribution it is possible to extract a statistical error. When the bias, which is the difference between the mean of the bootstrap distribution and the original fit, is small, the statistical uncertainty can be extracted from the 95% bootstrap confidence interval [29]. This interval is shown in Fig. 3.7, and will be used as the statistical error in the following.

3.5 Extrapolating data

The extrapolation technique was used in Paper A, B, C and D. In this section the results from our exploratory study of higher-order corrections to the

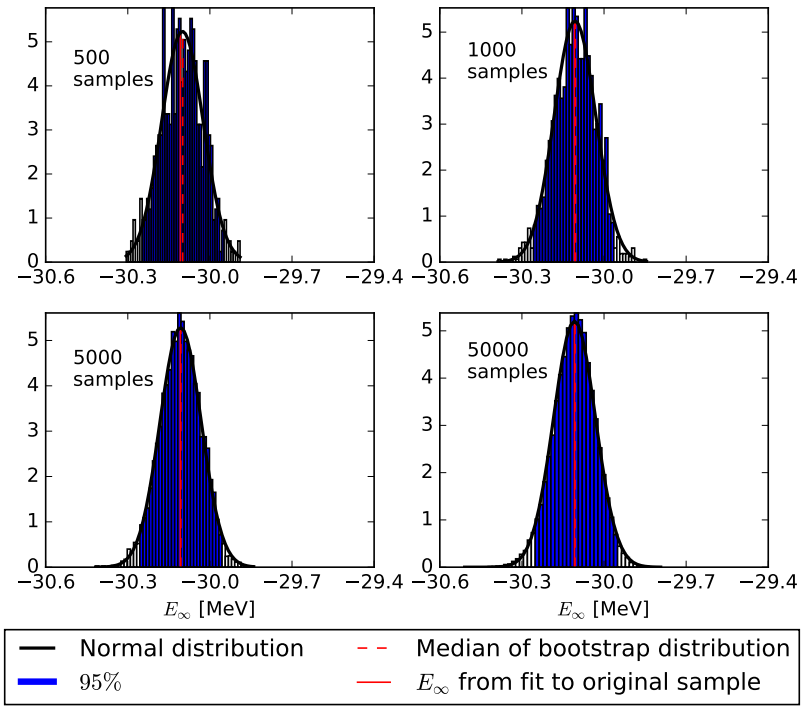

Figure 3.7: *Bootstrap distribution of E_∞ for different number of bootstrap samples obtained from resampling. The data is from a calculation of ^{6}Li with NNLOopt. Only datapoints with $\Lambda_{UV} > 1300$ MeV are included in the original sample that consisted of 72 unique data points.*

LO IR term, presented in Paper C, will work as an example on how the extrapolation is applied.

The technical improvements of the shell model code, presented in Paper C, opens up the opportunity to study the performance of the extrapolation for many-body systems in large model spaces, where the results are close to converged. A clear indication that the IR and UV corrections need to be studied further is revealed in Fig. 3.8 where we show that the extrapolated value of E_∞ is above the lowest computed energies. This result indicates that something is missing in the extrapolation, since according to the variational principle the computed result will always be above the true ground-state energy.

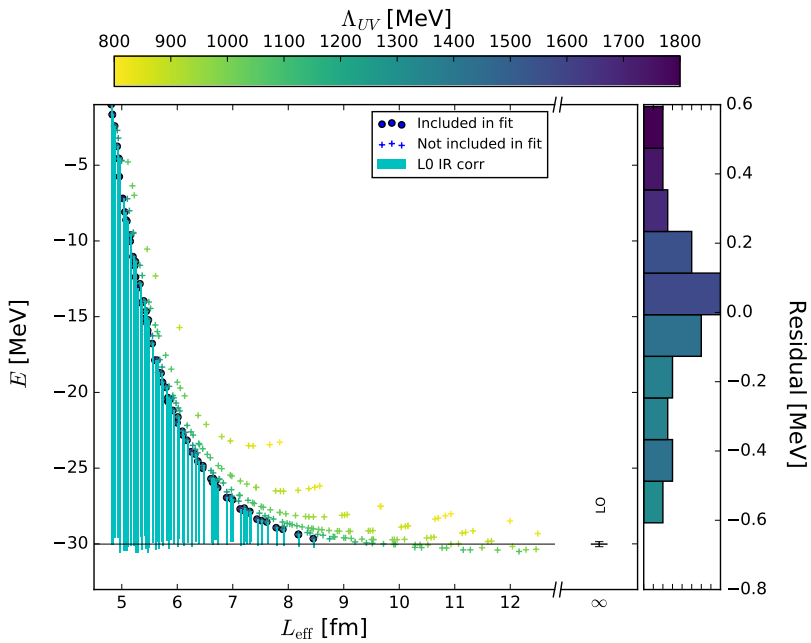

Figure 3.8: *Ground-state energy of* ^{6}*Li computed with NNLOopt [13]. Data points with* $\Lambda_{UV} > 1300$ *MeV are included in a LO IR fit. Vertical lines denote the correction* $E_{\text{LO}}^{\text{corr}}$ *of each data point. The residuals from the fit are shown in the right panel with the color of each bar determined by the mean* Λ_{UV} *of data in that interval. The errorbar is computed with the bootstrap method.*

In the literature there are various suggestions of higher order effects that may be important in the extrapolation. In particular, there are discussions of a NLO IR correction term [24] and an UV term [18]. The NLO IR-correction

has the suggested form

$$E_{\mathrm{IR,NLO}}^{\mathrm{corr}} = (BL + C)e^{-4k_\infty L}.$$

By including this term and studying the correlation matrix of the fitting parameters, we conclude that the NLO IR term was highly correlated with the LO one. Consequently, adding this NLO term will not capture any relevant new features in the fit.

In Ref. [18] a phenomenological UV correction term was suggested,

$$E_{\mathrm{UV}}^{\mathrm{corr}} = A_1 e^{-2(\Lambda_{UV}/\lambda)^2}.$$

When this term was added to the extrapolation the fitted parameter E_∞ became too large. This result is not surprising. The data points closest to the variational minimum are not the ones with the highest Λ_{UV}, (see Fig. 3.6). Consequently, these data points receive a large correction and the new UV-term pushes the extrapolation parameter E_∞ too far below the variational minimum. An example is shown in Fig. 3.9, where this term is included in the fit.

What is then the most relevant NLO correction? By studying the residuals of the IR LO extrapolation, shown in Fig. 3.10, a clear $N_{\max}$-dependence can be seen. Based on this finding we suggested in Paper C to add a UV/IR cross-term on the form,

$$E_{\mathrm{cross}}^{\mathrm{corr}} = A_2 e^{-L_{\mathrm{eff}}\Lambda_{UV}/d_1},$$

to the IR LO correction. The exponent in this expression can be written as

$$\frac{L_{\mathrm{eff}}\Lambda_{UV}}{d_1} = \frac{\tilde{N}(A, N_{\max}, \pi)^2}{d_1}.$$

A cross-term on the form $e^{-\sqrt{L_{\mathrm{eff}}\Lambda_{UV}}/d_1}$ can with the same arguments also be considered.

The inclusion of a Λ_{UV}-dependent term allows us to include data that is not completely UV-converged. This is an improvement compared to the pure IR-correction an is of particular importance in large systems where the results are further from converged. However, we still require $\Lambda_{\mathrm{UV}} \gg \Lambda_{\mathrm{EFT}}$.

In Fig. 3.9 the three suggested NLO correction terms are used for ^{6}Li. Considering the size of the residuals, the extrapolated values, and the statistical errors it seems clear that the cross-term provides the best fit. Although the cross-term improves the fit substantially, it does not completely

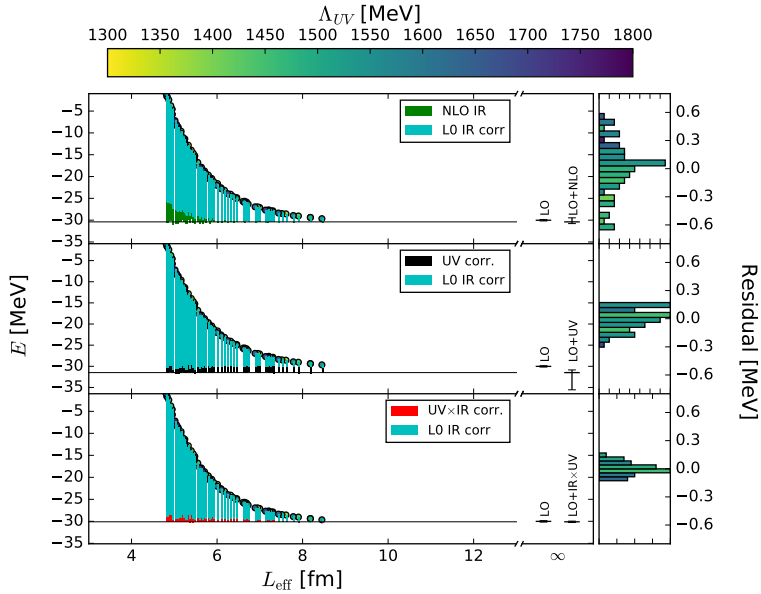

Figure 3.9: *The three suggested extrapolation schemes are tested for* ^{6}*Li computed with NNLOopt and only including data with* $\Lambda_{UV} > 1300$ *MeV. The errorbars are computed with the bootstrap method.*

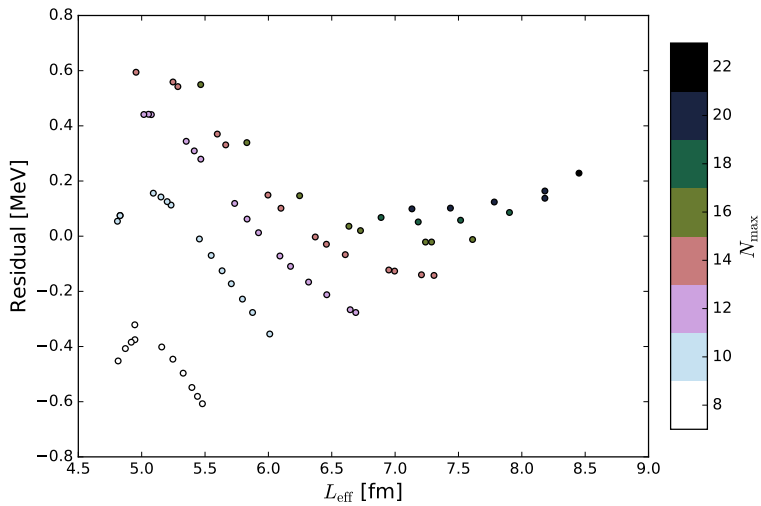

Figure 3.10: *Residuals from a LO IR fit of* ^{6}*Li data computed with NNLOopt [13]. Data with* $\Lambda_{UV} > 1300$ *MeV was included in the fit.*

resolve the issue of extrapolating E_∞ to a too high value. This finding is demonstrated in Fig. 3.11, where the fitted E_∞ is plotted together with the variational minima for a number of $N_{\max}$-truncations. This truncation implies a selection of data limited to $N_{\max} \leq N_{\max,\mathrm{cut}}$. The performance for smaller values of $N_{\max}$ is relevant to understand the applicability of the extrapolation method to larger systems. The fit with the cross term is closer to the variational minimum than the previous resluts with just the LO IR term, but we find that it is still 400 keV above in the largest model space. To resolve this issue, the extrapolation needs to be studied further. In particular, the treatment of the dependence on Λ_{UV} needs a better understanding.

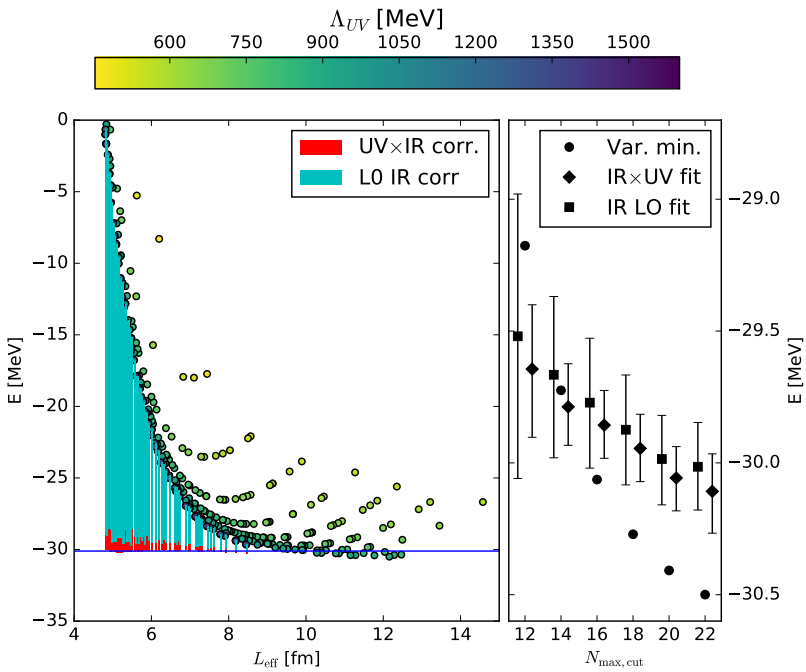

Figure 3.11: ^{6}*Li computed with NNLOopt. The left panel shows the extrapolation including all datapoints with* $\Lambda_{UV} > 1300$ *MeV. The right panel shows the extrapolated results and the variational minima for different* $N_{\max}$*-truncations.The errorbars are computed with the bootstrap method.*

Chapter 4

Observables and two-body operators in the NCSM

An advantage of the NCSM compared to some other methods is the ability to obtain microscopic wave functions. From the wave functions different observables can be computed. This can be achieved by utilizing the second quantization formalism, already introduced in Chap. 2. In second quantization the expectation value of an operator can be written as a product of a transition density matrix and matrix elements pf the operator in a sp basis. The aim of this chapter is to introduce the transition density matrix in more detail and present how it can be constructed and applied to compute observables. The final section is based on our work presented in Paper D, where we applied our efficient transition density code to compute nucleon-nucleon distances in ^{6}He to study the core-swelling effect.

4.1 Observables in second quantization

Many observables can be written as one- or two-body operators. In this section the focus will be on one-body operators. However, in the end the formalism will also be generalised to two-body operators. A one-body operator acts on the coordinates, including spin, of only one nucleon at a time. The total effect of a one-body operator on a many-body state is obtained by summing the contributions from the actions on the individual particles. For example, the total kinetic energy is the sum of the kinetic energies of the individual nucleons.

In second quantization a one-body spherical tensor operator of rank λ,

with projection quantum number μ, can be expressed as [8]

$$T_{\lambda\mu} = \sum_{\alpha,\beta} \langle\alpha| T_{\lambda\mu} |\beta\rangle \, a^\dagger_\alpha a_\beta, \tag{4.1}$$

where we used the notation introduced in Sec. 2.1. As a reminder, our sp states are either HO functions labeled with small letters $a = [n_a, l_a, j_a]$ or sp states that include the projection quantum numbers labeled with Greek letters, $\alpha = [a, m_a]$. The matrix elements $\langle\alpha| T_{\lambda\mu} |\beta\rangle$ completely characterize the operator. However, the many-body aspect is probed by the latter term, $a^\dagger_\alpha a_\beta$.

To compute the observable for a many-body system, the operator in Eq. (4.1) will operate on a many-body state, which results in

$$\langle\Lambda_f J_f M_f| T_{\lambda\mu} |\Lambda_i J_i M_i\rangle = \sum_{\alpha,\beta} \langle\alpha| T_{\lambda\mu} |\beta\rangle \left\langle\Lambda_f J_f M_f\right| a^\dagger_\alpha a_\beta \left|\Lambda_i J_i M_i\right\rangle, \tag{4.2}$$

where Λ corresponds to additional quantum numbers needed to characterize the state. The matrix element,

$$\rho_{\alpha\beta} = \left\langle\Lambda_f J_f M_f\right| a^\dagger_\alpha a_\beta \left|\lambda_i J_i M_i\right\rangle, \tag{4.3}$$

$\left\langle\Lambda_f J_f M_f\right| a^\dagger_\alpha a_\beta \left|\lambda_i J_i M_i\right\rangle$, defines the uncoupled, one-body transition density matrix. In this formalism the one-body operator matrix elements are computed independently of the transition properties of the many-body states. Similarly, if the transition densities are available they can be used to evaluate the expectation value of different one-body operators.

The Wigner-Eckart theorem states that it is possible to write a matrix element as a product of a factor dependent only on the projection quantum number, i.e. the geometric orientation of the z-axis, and another factor that contains the dependence on the dynamics of the operator [30]. The Wigner-Eckart theorem can be applied to the one-body operator in Eq. (4.1) [8],

$$T_{\lambda\mu} = \widehat{\lambda}^{-1} \sum_{a,b} \langle a\|T_\lambda\|b\rangle \, [a^\dagger_a \tilde{a}_b]_{\lambda\mu}, \tag{4.4}$$

where $\widehat{\lambda} = \sqrt{2\lambda + 1}$ and the $\tilde{a}_b$ is an annihilation operator with the proper behaviour of a spherical tensor of rank j_a. The tilde operator is defined as

$$\tilde{a}_\alpha \equiv (-1)^{j_a + m_\alpha} a_{a,-m_a}.$$

In addition, $\langle a \| T_\lambda \| b \rangle$ is the reduced single-particle matrix element.

The Wigner-Eckart theorem can also be applied to Eq. (4.2), yielding an expression in reduced form,

$$\langle \Lambda_f J_f \| T_\lambda \| \Lambda_i J_i \rangle = \sum_{a,b} \widehat{\lambda}^{-1} \langle a \| T_\lambda \| b \rangle \left\langle \Lambda_f J_f \middle\| [a_a^\dagger \tilde{a}_b]_\lambda \middle\| \Lambda_i J_i \right\rangle \tag{4.5}$$

where $\left\langle \Lambda_f J_f \middle\| [a_a^\dagger \tilde{a}_b]_\lambda \middle\| \Lambda_i J_i \right\rangle$ is the reduced one-body transition density. The reduction removes the dependence on the projection quantum number. Consequently, the number of matrix elements and transition densities are smaller.

The treatment of the two-body operators, that depend on the coordinates of pairs of nucleons, is analogous. The second quantization formalism can again be applied to two-body operators and matrix elements of a two-body operator, $T^{(2)}_{\lambda\mu}$, can be expressed

$$\left\langle \Lambda_f J_f M_f \middle| T^{(2)}_{\lambda\mu} \middle| \Lambda_i J_i M_i \right\rangle = \sum_{\alpha,\beta,\gamma,\delta} \left\langle \alpha\beta \middle| T^{(2)}_{\lambda\mu} \middle| \gamma\delta \right\rangle \left\langle \Lambda_f J_f M_f \middle| a^\dagger_\alpha a^\dagger_\beta a_\gamma a_\delta \middle| \Lambda_i J_i M_i \right\rangle . \tag{4.6}$$

Similarly to the one-body case, the two-body operator can be expressed in reduced form.

4.2 Transition densities in the NCSM

The computational challenge is the computation of transition densities from large-dimension many-body states. In the NCSM these are expansions in a SD basis,

$$|\Lambda A J M\rangle = \sum_{i=0}^{A} c_i \, |\phi_i\rangle \, , \tag{4.7}$$

where ϕ_i consist of A HO sp states that together satisfy the energy truncation, $N_{\max}$, and have a total $M = \sum_{i=1}^{A} m_i$.

The most time-consuming part of computing transition densities is to find all connections between the many-body states. Inserting the expansion (4.7) in the one-body transition density (4.3), we obtain

$$\rho_{\alpha\beta} = \sum_{i=0}^{A_f} c_f \sum_{j=0}^{A_i} c_i \left\langle \phi_f^{J_f M_f} \middle| a^\dagger_\alpha a_\beta \middle| \phi_i^{J_i M_i} \right\rangle .$$

To find all the connections the following recipe can be applied:

1. Loop over the basis states (i) of the ket state.
2. Loop over and remove, one at a time, the sp states β that are present in the many-body basis state $\left|\phi_i^{J_i M_i}\right\rangle$
3. Insert a sp state α in the intermediate $(A-1)$ many-body state such that the resulting A many-body state exists in the final many-body basis, i.e., that it has $M = M_f$ and satisfies the energy truncation,$N \leq N_{\max}$.
4. Find the index (f) of the resulting many-body state, $\left|\phi_f^{J_f M_f}\right\rangle$
5. Accumulate $c_i c_f$ for the combination of $\alpha\beta$.

In the case of two-body transition densities, there are two additional steps. Firstly, after removing the first sp state, another state needs to be removed. Secondly, an additional sp state needs to be inserted to find a connection to a final many-body state. The number of connections grows rapidly with $N_{\max}$, which was demonstrated in Fig. 2.2 that shows the number of non-zero matrix elements as a function of $N_{\max}$. However, the sp states can be coupled and the transition density can be obtain in reduced form, which will decrease the number of connections. The code, ANICRE, that we developed to compute one- and two-body transition densities in the NCSM is presented in Paper D.

4.3 Nucleon-nucleon distances

As a test of the computed two-body transition densities, we studied the nucleon-nucleon distance, r_{N-N}, which corresponds to the expectation value of a two-body operator. The two-body matrix elements of the operator can be computed from matrix elements of the HO Hamiltonian by using the relation

$$H_{HO}^{\text{rel}} = \sum_{i<j=1}^{A} H_{HO}^{\text{rel}}(i,j) = \sum_{i<j=1}^{A} \frac{(\vec{p}_i - \vec{p}_j)^2}{2m_N A} - \frac{m\Omega^2}{2A}(\vec{r}_i - \vec{r}_j), \tag{4.8}$$

where i and j corresponds to particle i and j, respectively. The transition densities are computed separately for neutron-neutron, proton-proton and proton-neutron pairs. Therefore, it is possible to compute the nucleon-nucleon distance for a specific pair of particles. In order to extract the mean pair distance the resulting value needs to be normalized with respect to the number of pairs of particles.

4.4 Core-swelling in ^{6}He

Having developed the ability to to compute nucleon-nucleon distances we can study a very interesting physics question, namely the core-swelling effect in halo systems. Consider, e.g., the ground-state of ^{6}He. In the three-body halo picture of ^{6}He, the α core is surrounded by two valence nucleons. The attractive behaviour of the nuclear force between the valence nucleons and the ones in the core will cause an enlargement of the core compared to a free α particle. This enlargement is called the core-swelling effect.

The size of the core in a halo system is an important input to cluster models, since in such a model the core is one of the constituents. The importance of core-swelling is obvious when considering cluster model calculations of the radius, in for example ^{6}He [31, 4]. We will use the NCSM to study the core-swelling from a microscopic perspective.

One way of estimating the core-swelling effect is to compute the proton-proton distance in ^{4}He and compare it with the corresponding distance in ^{6}He. The average nucleon-nucleon distances in ^{6}He are plotted as a function of L_{eff} in Fig. 4.1. The neutron-neutron distance is the largest distance, and it is clear that our results are far from IR-converged, which is expected since the distribution of the neutrons is particularly sensitive to the asymptotic behaviour of the wave function. However, the proton-proton distance is much smaller and better converged. These results are in more detail presented in Paper D.

The proton-proton distance in ^{6}He can now be compared to the corresponding distance in ^{4}He, both plotted in Fig. 4.2. Clearly, there is a significant enlargement of the core in ^{6}He. An estimate of the size of the core-swelling effect can be extracted from the extrapolated values. Using the NNLOopt interaction the resulting core-swelling effect in ^{6}He is $\approx 9\%$. The extrapolation in Fig. 4.2 is performed utilizing the framework introduced in Chap. 3 and the IR correction derived for the radius [18],

$$r^2(L) \approx r_\infty^2[1 - (c_0\beta^3 + c_1\beta))e^{-\beta}] \quad \text{and} \quad \beta = 2k_\infty L, \tag{4.9}$$

is used. It is notable that the expression for the IR correction of the radius seems to work for the extrapolation of the nucleon-nucleon distance.

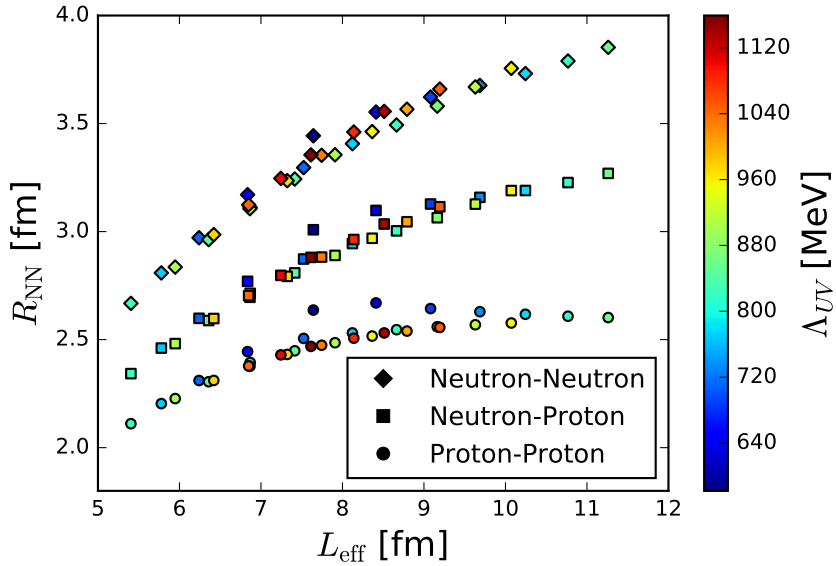

Figure 4.1: *Nucleon-nucleon distance in ^{6}He computed with NNLOopt [13]. Data points with $N_{\max} \leq 14$ are included*

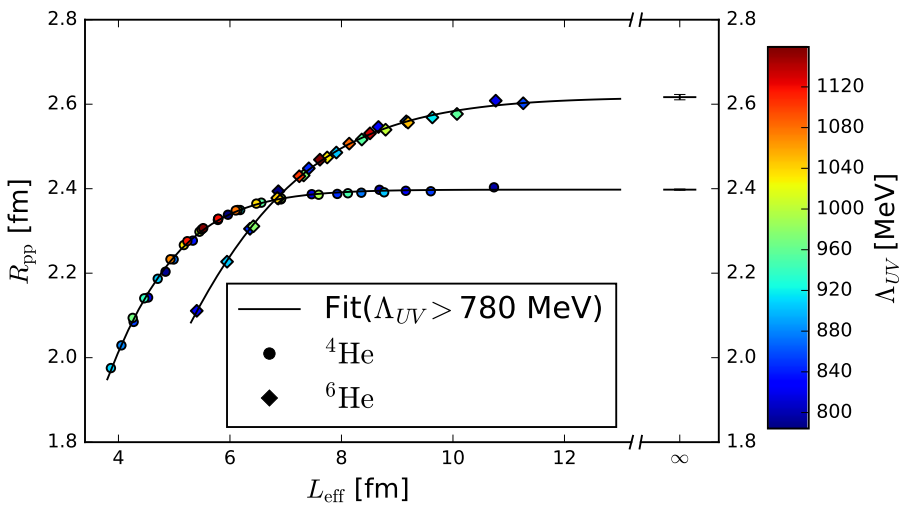

Figure 4.2: *Proton-proton distance in ^{6}He and ^{4}He computed with NNLOopt [13]. The errorbars corresponds to the statistical uncertainty in the fit.*

Chapter 5

Microscopic description of a three-body cluster system

The ability to compute translationally invariant wave functions in the NCSM opens up the possibility to study the structure of the nucleus in detail. When approaching the nuclear dripline a variety of cluster structures emerge that are interesting to study from an *ab initio* perspective. In this thesis we are particularly interested in the appearance of three-body (Core+N+N) structures as found e.g. in Borromean halo states of ^{6}He and ^{11}Li. Such states have earlier been described with phenomenological cluster models [4].

In Paper A we developed a framework to study the three-body clusterization from a microscopic perspective by calculating translationally invariant cluster form factors for the Core+N+N channel. A brief overview of the derivation will be given in this chapter. In this framework, the ^{6}He ground state was studied as a three-body system consisting of a ^{4}He-core and in the final section of this chapter some of the results will be presented. A more detailed derivation of the Core+N+N framework is presented in Ref. [32].

5.1 Overlap functions

In order to introduce overlap functions in general terms it is natural to start with the definition of the two-body overlap function. Consider a nucleus A that is composed of two clusters, B and C. The overlap function then involves the integral over three wave functions, $\psi_A^{J_A M_A}$, $\psi_B^{J_B M_B}$ and $\psi_C^{J_C M_C}$. The nucleus A consists of the nucleons from B and C, $A = B + C$. The J_i and M_i are the spin and the projection quantum numbers, respectively.

The integral is over the internal coordinates of the wave functions B and C, which results in the overlap function being a function of the relative coordinate $\vec{r}$, between the clusters B and C. The general definition of the two-body overlap function is

$$u^{J_A M_A}_{J_B M_B, J_C M_C}(\vec{r}) = \int d\vec{x}_B d\vec{x}_C \; \psi_A^{J_A M_A}(\vec{r}, \vec{x}_B, \vec{x}_C) \psi_B^{J_B M_B *}(\vec{x}_B) \psi_C^{J_C M_C *}(\vec{x}_C),$$

where x_B (x_C) are the intrinsic coordinates of B (C) and in addition includes the spin and isospin coordinates. Note that the overlap function is a non-observable, it can not be written as the expectation value of an Hermitian operator. Non-observable properties are model-dependet and can change e.g. under unitary transformations.

The two-body overlap function was studied in the NCSM by P. Navrátil [33]. The formalism presented in Ref. [33] was relevant for our work and is best introduced by studying the simplest two-body overlap function, namely the Core+N obtained from

$$u^{A\lambda JT}_{(A-1)I_1T_1, I_2T_2}(\eta) = \langle A\lambda JT | \mathcal{A}_{A-1,1} \Phi^{A\lambda JT}_{(A-1)\lambda_1 I_1 T_1, I_2 T_2}; \delta_\eta \rangle, \tag{5.1}$$

here expressed in braket notation. We will continue to use the braket notation in the following. The bra in this expression corresponds to an A-nucleon state with total spin (isospin) J (T) and an additional quantum number λ that might be needed to characterize the eigenstate. The ket corresponds to an antisymmetrized two-body cluster state with fixed relative distance,η. The two clusters are an $(A-1)$-nucleon state with quantum numbers I_1T_1, and a single-nucleon state with I_2T_2 as quantum numbers. This general notation will be used although it is clear that $I_2 = T_2 = \frac{1}{2}$ in our case. The A-nucleon state and the (A-1) cluster will be described in a SD basis. The distance between the two clusters is described by the normalized Jacobi coordinate,

$$\vec{\eta} = \sqrt{\frac{(A-1)}{A}} \left[\frac{1}{A-1} \sum_{i=1}^{A-1} \vec{r}_i - \vec{r}_A \right],$$

where $\vec{r}_i$ is the absolute coordinate of particle i. Furthermore, $\mathcal{A}_{A-1,1}$ is a cluster antisymmetrizer that ensures antisymmetrization with respect to exchange of nucleons between the clusters. The Jacobi coordinate $\vec{\eta}$ is shown in Fig.5.1 (a).

In Paper A we generalized the computation of overlap functions to three-body systems. We considered a large cluster with $A-a$ nucleons and

two small clusters with a_2 and a_3 nucleons, respectively. This implies that $a = a_2 + a_3$. In this case, another set of Jacobi coordinates need to be introduced, corresponding to the vector $\vec{\eta}$ between the large and the center of the small clusters, and the vector $\vec{\nu}$ between the two small clusters,

$$\begin{aligned}\vec{\eta} &= \sqrt{\frac{(A-a)a}{A}}\left[\frac{1}{A-a}\sum_{i=1}^{A-a}\vec{r}_i - \frac{1}{a}(\vec{r}_{A-a+1} + \vec{r}_A)\right] \\ \vec{\nu} &= \sqrt{\frac{1}{2}}\left[\frac{1}{a_2}\sum_{i=A-a+1}^{A}\vec{r}_i - \frac{1}{a_3}\sum_{i=A-a_3+1}^{A}\vec{r}_i\right].\end{aligned} \tag{5.2}$$

This coordinate system is shown in the lower panel of Fig. 5.1. The third cluster with a_3 nucleons is characterized by the additional quantum numbers I_3T_3 and it is now possible to define a three-body cluster overlap function:

$$\begin{aligned}&u^{A\lambda JT}_{(A-a)\lambda_1 I_1 T_1, a_2\lambda_2 I_2 T_2, a_3\lambda_3 I_3 T_3}(\eta,\nu) \\ &= \langle A\lambda JT|\mathcal{A}_{A-a,a_2,a_3}\Phi^{AJT}_{(A-a)\lambda_1 I_1 T_1, a_2\lambda_2 I_2 T_2, a_3\lambda_3 I_3 T_3}; \delta_\eta\delta_\nu\rangle.\end{aligned} \tag{5.3}$$

The ket is an antisymmetrized three-body cluster wave function where the relative distances are fixed.

Acting with the three-cluster antisymmetrizer on the A-body state to the left, will simply give a combinatorial factor since the A-body state is already fully antisymmetric. Furthermore, the Dirac δ-functions can be expanded in terms of radial HO functions and in that way the overlap function can be expressed in a HO basis. This results in the expansion:

$$\begin{aligned}&u^{A\lambda JT}_{(A-a)\lambda_1 I_1 T_1, a_2\lambda_2 I_2 T_2, a_3\lambda_3 I_3 T_3}(\eta,\nu) = \\ &\sum_{\substack{n_\eta l_\eta \\ n_\nu l_\nu}} R_{n_\eta l_\eta}(\eta) R_{n_\nu l_\nu}(\nu)\langle A\lambda JT|\mathcal{A}_{A-a,a_2,a_3}\Phi^{AJT}_{(A-a)\lambda_1 I_1 T_1, a_2\lambda_2 I_2 T_2, a_3\lambda_3 I_3 T_3}; n_\eta l_\eta, n_\nu l_\nu\rangle.\end{aligned} \tag{5.4}$$

5.2 Derivation of Core+N+N overlap function

The aim of this section is to highlight the main steps in the derivation of an expression for the Core+N+N overlap function with matrix elements between many-body states in an SD basis, which can be computed from

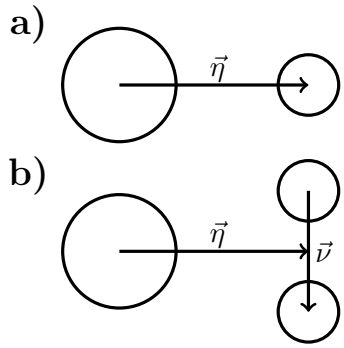

Figure 5.1: *The Jacobi coordinates used in the definition of the overlap functions. a) is the two-body cluster system and b) is the three-body cluster system.*

wave functions obtained in the NCSM. The derivation is presented in more detail in Paper A and Ref. [32]. The derivation can be summarized in a number of steps:

1. Introduce three-body cluster wave functions in relative and absolute coordinates.

2. Relate the overlap function in relative coordinates to a corresponding overlap function expanded in a SD basis

3. Expand the overlap function in mixed coordinates (absolute for particles in the large cluster an relative for the others) and apply the Talmi-Moshinsky transformation to the relative ones.

4. Express the sp states in terms of field creation operators and perform recoupling of spins.

5. Integrate over the intrinsic sp coordinates of the large cluster and perform a summation over the sp quantum numbers, thus yielding an expression for the Core+N+N overlap function.

5.2.1 General three-body overlap function

The first step is to define the three-body cluster wave function in relative Jacobi coordinates. In the end, the derivation will focus on the Core+N+N channel where the two smaller clusters consist of only one nucleon each, but as a start the general case will be considered. To treat the entire system

microscopically, another set of relative coordinates needs to be introduced to describe the relative distance between the nucleons in each cluster. These coordinates are sets of normalized Jacobi coordinates. In cluster 1 they are defined as

$$\begin{aligned}
\vec{\xi}_1 =& \sqrt{\frac{1}{2}}(\vec{r}_1 - \vec{r}_2) \\
\vec{\xi}_2 =& \sqrt{\frac{2}{3}}\left[\frac{1}{2}(\vec{r}_1 + \vec{r}_2) - \vec{r}_3\right] \\
&\vdots \\
\vec{\xi}_{A-a-1} =& \sqrt{\frac{A-a-1}{A-a}} \\
&\times \left[\frac{1}{A-a-1}(\vec{r}_1 + \vec{r}_2 + \ldots + \vec{r}_{A-a-1}) - \vec{r}_{A-a}\right]
\end{aligned}$$

The intrinsic coordinates in clusters 2 and 3 are defined in the same way, but denoted $\vec{\mu}_i$ and $\vec{\rho}_i$, respectively. All relative coordinates are shown in Fig. 5.2 for a specific example. In the following, $\boldsymbol{\xi}$ will be used to denote all $\vec{\xi}_i$ vectors and $\boldsymbol{\mu}$, $\boldsymbol{\rho}$ will denote the intrinsic coordinates of clusters 2 and 3, respectively. A coordinate corresponding to the center of mass of the

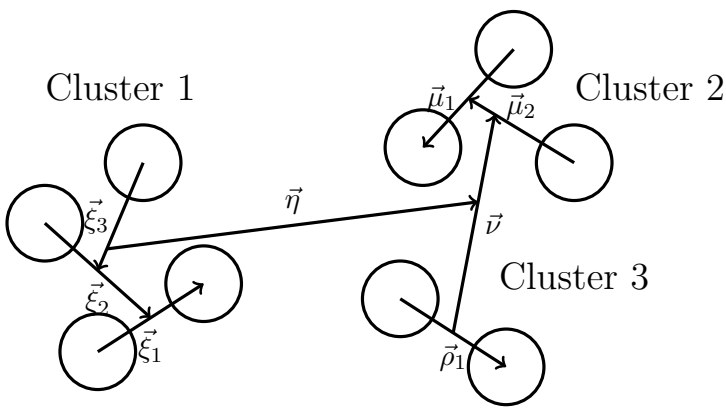

Figure 5.2: *Sketch of the coordinate systems in a three-body cluster system*

A-body system is also needed

$$\vec{\xi}_0 = \sqrt{\frac{1}{A}}(\vec{r}_1 + \vec{r}_2 + \ldots + \vec{r}_A).$$

Introducing a shorthand notation for the The cluster wave function can now be defined in relative coordinates for a fixed set of relative distances defined by η' and ν'

$$\begin{aligned}
\left\langle \boldsymbol{\xi}\eta'\vec{\eta}\boldsymbol{\mu}\nu'\vec{\nu}\boldsymbol{\rho}\boldsymbol{\sigma}\boldsymbol{\tau}\right| \Phi_\alpha^{AJMTM_T};\delta_\eta\delta_\nu\big\rangle &= \sum (l_\eta m_\eta l_\nu m_\nu|LM_L) \\
&\times (I_2M_2I_3M_3|I_{23}M_{23})(I_1M_1I_{23}M_{23}|SM_S)(LM_LSM_S|JM) \\
&\times (T_2M_{T_2}T_3M_{T_3}|T_{23}M_{T_{23}})(T_1M_{T_1}T_{23}M_{T_{23}}|TM_T)\frac{\delta(\eta-\eta')}{\eta\eta'}\frac{\delta(\nu-\nu')}{\nu\nu'} \\
&\times Y_{l_\eta m_\eta}(\hat{\eta})Y_{l_\nu m_\nu}(\hat{\nu})\left\langle \boldsymbol{\xi},\sigma_1\ldots\sigma_{A-a},\tau_1\ldots\tau_{A-a}\right| a_1\lambda_1I_1M_1T_1M_{T_1}\big\rangle \\
&\times \left\langle \boldsymbol{\mu},\sigma_{A-a+1}\ldots\sigma_{A-a_3}\tau_{A-a+1}\ldots\tau_{A-a_3}\right| a_2\lambda_2I_2M_2T_2M_{T_2}\big\rangle \\
&\times \left\langle \boldsymbol{\rho},\sigma_{A-a_3+1}\ldots\sigma_A\tau_{A-a_3+1}\ldots\tau_A\right| a_3\lambda_3I_3M_3T_3M_{T_3}\big\rangle\,,
\end{aligned} \tag{5.5}$$

where each cluster has a total angular momentum I_i, a total isospin T_i and an additional quantum number λ_i to distinguish the eigenstate. Together the three clusters form an A-body system with total angular momentum J and a total isospin T, with the projections M and M_T, respectively. Furthermore, $\boldsymbol{\sigma} = [\sigma_1,\ldots\sigma_A]$ are the spin coordinates and $\boldsymbol{\tau} = [\tau_1,\ldots\tau_A]$ the isospin ones. The quantum numbers for the three-cluster state in LS-coupling are combined into one index $\alpha = [(A-a)\lambda_1I_1T_1, a_2\lambda_2I_2T_2, a_3\lambda_3I_3T_3 : LS]$.

In addition, a three-body cluster wave function with mixed coordinates also needs to be introduced. In this wave function the largest cluster is expressed in sp coordinates so that it can be expanded in a SD basis. This definition of the cluster wave function is needed to use NCSM eigenstates to describe the largest cluster. Since sp coordinates introduces a dependence on the CM of the largest cluster, the coordinate η also needs to be transformed to sp coordinates.

To relate the overlap function in relative coordinates to the corresponding one in sp coordinates it is possible to use Eq (2.6) on the composite state and on the large cluster state, both expanded in a SD basis. This factors out the CM motion. Consequently, it is possible to apply the Talmi-Moshinsky transformation [34] to finally get the relation

$$\begin{aligned}
&\left\langle A\lambda JMTM_T\right| \mathcal{A}_{A-a,a_2,a_3}\Phi_\alpha^{AJMTM_T};n_\eta l_\eta,n_\nu l_\nu\big\rangle \\
&= \frac{{}_{\text{SD}}\left\langle A\lambda JMTM_T\right| \mathcal{A}_{(A-a),a_2,a_3}\Phi_\alpha^{AJMTM_T};n_\eta l_\eta,n_\nu l_\nu\big\rangle_{\text{SD}}}{\langle n_\eta l_\eta 00 l_\eta|\,00 n_\eta l_\eta l_\eta\rangle_{\frac{a}{A-a}}},
\end{aligned} \tag{5.6}$$

where the denominator is a general HO bracket from the Talmi-Moshinksy transformation.

5.2.2 Core+N+N overlap function

Until now, the cluster-state notation has been valid for a rather general three-body system. In the following it will be assumed that the two smaller clusters (2 and 3) only consist of one nucleon each. Still, the spin (isospin) labels I_2 and I_3 (T_2 and T_3) will be kept, although they obviously correspond to spin (isospin) $\frac{1}{2}$.

The next step in the derivation, as summarized in the bullet list on page 41, is to expand the overlap function in mixed coordinates, corresponding to the coordinates in the mixed three-body cluster wave function. At this stage it is possible to apply the Talmi-Moshinsky transformation to transform the two HO states, corresponding to cluster 2 and 3, in relative coordinates to HO states in absolute coordinates. By applying spin-recouplings and rewriting the coordinates as field creation operators acting on a vacuum state an intermediate expression of the three-body overlap function can be derived. This expression can be simplified by integrating over the sp coordinates of the large cluster and performing the summation over the sp quantum numbers. The resulting expression for the three-body overlap function is

$$
\begin{aligned}
u_\alpha^{A\lambda JT}(\eta,\nu) = \sum_{\substack{n_\eta l_\eta \\ n_\nu l_\nu \ldots}} & \frac{R_{n_\eta l_\eta}(\eta) R_{n_\nu l_\nu}(\nu)}{\langle n_\eta l_\eta 00 l_\eta |\, 00 n_\eta l_\eta l_\eta \rangle_{\frac{2}{A-2}}} (-1)^{3I_1+I_{23}+J_{ab}-T_{23}-S+L} \\
& \times \langle n_a l_a n_b l_b L |\, n_\eta l_\eta n_\nu l_\nu L \rangle_1 \, \frac{\hat{L}\hat{S}\hat{J}_{ab}^2 \hat{j}_a \hat{j}_b}{\hat{J}\hat{T}} \begin{Bmatrix} L & I_{23} & J_{ab} \\ I_1 & J & S \end{Bmatrix} \begin{Bmatrix} l_a & l_b & L \\ I_3 & I_2 & I_{23} \\ j_a & j_b & J_{ab} \end{Bmatrix} \\
& \times \, {}_{\mathrm{SD}}\left\langle A\lambda JT \middle\| \left[a^\dagger_{n_a l_a j_a t_a} a^\dagger_{n_b l_b j_b t_b} \right]^{J_{ab} T_{ab}} \middle\| (A-2)\alpha_1 I_1 T_1 \right\rangle_{\mathrm{SD}} ,
\end{aligned}
\tag{5.7}
$$

where the last matrix element is a doubly reduced, non-diagonal transition density computed from microscopic wave functions obtained in the NCSM. This transition density is similar to the transition densities described in Chap. 4 although this one connects states of two different nuclei with A and $(A-2)$ nucleons, respectively.

5.3 Clusterization of ^{6}He

We are now in a position to analyse the clusterization of ^{6}He by computing the overlap function between ^{6}He and an antisymmetric three-cluster state consisting of ^{4}He and two neutrons. This gives us the possibility to study the inherent cluster structure in the microscopically calculated wave functions. In this section we will show and discuss some of the results presented in Paper A.

5.3.1 Overlap functions

There are two different spin-channels for the overlap $\langle ^6\mathrm{He}(0^+)|^4\mathrm{He}(0^+) + n + n\rangle$, namely $S = L = 0$ and $S = L = 1$. Recall that S is obtained by coupling together I_1, I_2 and I_3, and L by coupling l_η and l_ν, where l_η and l_ν correspond to the angular momenta of the coordinates $\vec{\eta}$ and $\vec{\nu}$, respectively. The overlap functions for these two different channels are shown in Fig. 5.1. The most obvious thing to note is that the $S = L = 0$ channel is clearly dominating. This channel displays the characteristic shape of the two-neutron Borromean halo with a di-neutron and a cigar configuration. The di-neutron configuration corresponds to the two neutrons being close together but far away from the core, while the cigar configuration the neutrons are far from each other but their CM close to the core. This probability density is in agreement with earlier phenomenological cluster model calculations [4] and microscopic calculations done with a schematic interaction [35].

Very importantly, with this toolbox that we have developed it is now possible to study the origin of the observed clusterization. In Fig. 5.4 the overlap functions obtained in different $N_{\max}$ truncated model spaces are displayed. The panel in the top-left corner corresponds to a really tiny model space, $N_{\max} = 2$, but already here the clusterization is clearly visible. Compared to the panel in the bottom-left corner with a very large model space, $N_{\max} = 14$, there are no distinct differences in the structure. The only visible difference is that the overlap function in the larger model space has a larger radial extension. The conclusion drawn from these results is that the clusterization is driven by the Pauli principle, since in the tiny model space the only property of the wave function that is guaranteed to be captured is the antisymmetrization of the nucleons (due to the SD basis). Note that the $N_{\max} = 2$ model space is much too small to capture the physics of the interaction.

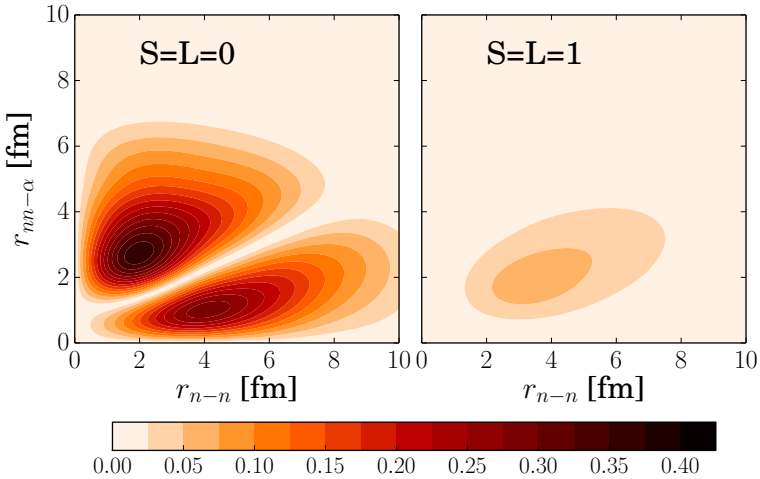

Figure 5.3: *Contour plot of the overlap function of* ^{6}*He. The left (right) panel corresponds to the* $S = L = 0$ *(*$S = L = 1$*) channel. This calculation is performed in a NCSM model space with* $\hbar\Omega = 20$ *MeV and* $N_{\max} = 14$ *. The interaction is I-N3LO with* $\Lambda_{\mathrm{SRG}} = 2.0$ *fm*$^{-1}$*.*

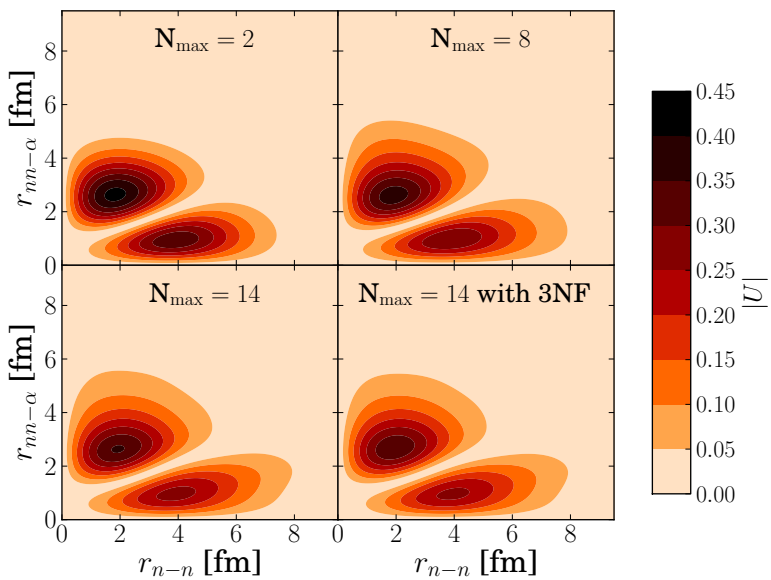

Figure 5.4: *The overlap function for the* $S = L = 0$ *channel. The wave functions are computed for increasing model spaces with* $\hbar\Omega = 16$ *MeV and I-N3LO with* $\Lambda_{\mathrm{SRG}} = 2.0$ *fm*$^{-1}$*. The wave functions obtained from a Hamiltonian including NN+3NF interactions are provided by R. Roth [36].*

5.3.2 Spectroscopic factors

An integrated measure of the amount of clusterization is the spectroscopic factor, which is the norm of the overlap function. It is worth reminding the reader that spectroscopic factors are non-observable quantities that change, e.g. under unitary transformations of the Hamiltonian. However, they are still important in phenomenological reaction theory as input for taking into account the structure of the atomic nuclei [37].

Projection on a hyperspherical harmonics basis

In order to study the spectroscopic factors we have chosen to project the three-body overlap functions onto a hyperspherical harmonics (HH) basis. This is done by first transforming to hypercoordinates $(\rho, \theta, \hat{\eta}, \hat{\nu})$ where $\eta = \rho\cos(\theta)$ and $\nu = \rho\sin(\theta)$. The overlap function in Eq. (5.7) can be written in hyperspherical coordinates,

$$u_\alpha^{A\lambda JT}(\theta, \rho) = \frac{1}{\rho^{5/2}} \sum_{K, l_\eta, l_\nu} \chi^{A\lambda JT}_{\alpha, K l_\eta l_\nu}(\rho) \psi_K^{l_\eta l_\nu}(\theta) \tag{5.8}$$

where

$$\begin{aligned} \chi^{A\lambda JT}_{\alpha, K l_\eta l_\nu}(\rho) = \rho^{5/2} \int_0^{\pi/2} d\theta' \sin^2\theta' \cos^2\theta' \psi_K^{l_\eta l_\nu}(\theta) \\ \times \sum_{n_\eta, n_\nu} C^{A\lambda JT}_{\alpha, n_\eta l_\eta, n_\nu l_\nu} R_{n_\eta l_\eta}(\theta', \rho) R_{n_\nu l_\nu}(\theta', \rho). \end{aligned} \tag{5.9}$$

The $\psi_K^{l_\eta l_\nu}(\theta)$ are the hyperangular basis functions [38] and K is the hyperangular momentum, which can be written as $K = l_\eta + l_\nu + 2n$ where $n = 0, 1, 2 \ldots$. The factor $C^{A\lambda JT}_{\alpha, n_\eta l_\eta, n_\nu l_\nu}$ contains all factors in Eq. (5.7) except the radial HO functions. The projection onto HH basis is presented with further details in Ref. [32].

Spectroscopic factors in ^{6}He

In Table 5.1 the weights for the five most important terms in the HH expansion are presented, together with the total spectroscopic factor. The first observation from this data is that the dominant term is the $K = 2$ and $l_\eta = l_\nu = 0$ one, in agreement with earlier calculations [35, 4]. This term is responsible for the characteristic two-peak structure shown in Fig. 5.3. One

Table 5.1: Relative weights (in %) of the HH expansion terms for the three-body channel form factor $\left\langle {}^6\mathrm{He}(0^+)|{}^4\mathrm{He}(0^+)+n+n\right\rangle$ calculated from NCSM wave functions. We compare results obtained with Hamiltonians including two-body forces only, and with two- plus three-body forces. The last row shows the total spectroscopic factor. We have used: I-N3LO, $\Lambda_{\mathrm{SRG}} = 2.0$ fm^{-1}, $\hbar\Omega = 20$ MeV and $N_{\max} = 14$. In addition, we have analysed a wave function computed with an N2LO 3NF [40], $\hbar\Omega = 16$ MeV, $\Lambda_{\mathrm{SRG}} = 2.0$ fm^{-1} that was provided by R. Roth [36].

Three-body channel			This work		Ref. [4]	Ref. [35]
K	$l_\eta = l_\nu$	$L = S$	NN	NN+3NF	(cluster)	(microscopic)
0	0	0	4.3	4.1	4.2	4.0
2	0	0	91.9	91.3	82.1	79.9
2	1	1	2.2	3.0	11.2	13.3
6	2	0	1.1	1.0	1.7	1.9
6	3	1	0.1	0.1	0.8	0.8
Spectroscopic factor:			1.3340	1.3284	0.9851	1.3957

detail that is important to note is that our total spectroscopic factor is larger then one. This is in agreement with the spectroscopic factors computed in a microscopic model presented in [35]. According to Timofeyuk [39] the fact that the spectroscopic factor is larger then unity is due to the movement of the CM of the cluster wave function and in Ref. [39] an upper limit of the spectroscopic factor for this system was derived to be $\frac{25}{16} \approx 1.56$, which is consistent with our results. In the cluster calculation [4], the wave functions are normalized with respect to the CM motion, therefore the spectroscopic factors sum up to unity.

Chapter 6

Summary of papers

In **Paper A**, we derived an expression for computing the translationally invariant overlap function for a core+N+N system starting from microscopic wave functions obtained in the NCSM using single-particle coordinates. In particular, we studied the two-neutron halo state in ^{6}He, using realistic nucleon-nucleon interactions, by computing the overlap function $\langle ^6\mathrm{He}(0^+)|\ ^4\mathrm{He}(0^+) + n + n\rangle$. By analysing this overlap function we demonstrated that the clusterization is driven by the Pauli principle. We also computed the spectroscopic functions in a Hyperspherical Harmonics basis.

The use of finite harmonic-oscillator model spaces introduces a model-space dependence of the NCSM results. To obtain infinite model-space results we need a way to correct for the model-space truncation. This truncation can in fact be viewed as the introduction of infrared (IR) and ultraviolet (UV) cutoffs. By working in the UV-converged regime and deriving the effect of the IR cutoff, corrections can be determined for several observables (at least to leading-order). Through applying these corrections we can extrapolate to converged results. In **Paper B**, we determined the infrared length scale of the NCSM model space, by equating the kinetic-energy eigenvalues in the NCSM basis with the corresponding energy spectrum of a hyper-radial well with Dirichlet boundary condition. We also demonstrated that we have indeed identified an accurate IR cutoff by extrapolating ground state energies from NCSM calculations for several light isotopes.

In **Paper C**, we presented new technical developments of the exact diagonalization method as implemented in the NCSM. These developments allow us to diagonalize very large model spaces, with basis dimensions exceeding 10^{10}. This gives us the ability to compute converged results for many-body systems with up to six particles with a bare chiral nucleon-

nucleon interaction. In particular, we presented results for ^{6}Li in model spaces up to $N_{\max} = 22$ and ^{10}B in model spaces up to $N_{\max} = 12$. We used this capability to perform an exploratory study of the IR and UV extrapolation of energies based on the length scale derived in Paper B. In particular, we investigated the effects of adding higher-order corrections, such as next-to-leading-order IR terms and a cross term dependent on both the UV and IR cutoff.

As a continuation of the work presented in Paper A, where we studied the clusterization of ^{6}He in a microscopic model, we investigated in **Paper D** the polarization of the α-core inside ^{6}He. To be specific, we computed the core-swelling effect by comparing the proton-proton distances in ^{6}He and ^{4}He. Nucleon-nucleon distances can be computed from two-body transition densities. A new code, ANICRE, was developed in order to efficiently compute one- and two-body transition densities from NCSM wave functions for very large model spaces. To achieve this goal, ANICRE, performs a pre-sorting of lists of allowed single-particle jumps and therefore succeeds to efficiently find the connections between the many-body states.

Chapter 7

Conclusion and Outlook

A large fraction of this work was devoted to the calculation of transition densities in the NCSM. We developed a code to efficiently compute one- and two-body transition densities from large-scale wave functions obtained in the NCSM. In addition, we used transition densities to study clusterization in light nuclei, and in particular the halo state of ^{6}He, by computing three-body overlap functions and the core-swelling effect.

Another component of this work involved corrections to results computed in finite oscillator model spaces. The framework to compute such corrections is rather new, and there has been a lot of progress during the last years, to which our work has contributed. This framework opens up the opportunity to compute, in a systematic way, basis-independent results for larger many-body systems than previously feasible.

To continue this line of research there are some obvious following steps: The transition density code, ANICRE, developed during this thesis has a large scope of applications and can be applied to other interesting operators as well. In particular, chiral EFT predicts the appearance of many-body currents in the interaction of nuclei with external probes. The computation of observables such as Gamow-Teller transition strengths in weak processes will require the ability to handle many-body operators. In addition, there is an ongoing project to develop a new NCSM code that, similarly to Antoine, computes matrix elements on-the-fly, although with the capability to handle three-body forces. In this code, ANICRE will play a crucial role and will be used as an essential ingredient.

Furthermore, the framework to compute three-body overlap functions can also be applied to larger systems. In particular, the study of ^{11}Li would be a natural continuation of the work presented in Paper A. In addition, as

previously suggested, further investigations of the corrections to the finite oscillator spaces are needed, to resolve some outstanding questions that were identified in this thesis.

References

[1] N Barnea et al. Effective Field Theory for Lattice Nuclei. *Physical Review Letters* **114**.5 (2015), 052501–5.

[2] P G Hansen and B Jonson. The Neutron halo of extremely neutron-rich nuclei. *Europhysics Letters* **4**.4 (1987), 409–414.

[3] I Tanihata et al. Measurements of Interaction Cross-Sections and Nuclear Radii in the Light P-Shell Region. *Physical Review Letters* **55**.24 (1985).

[4] M.V. Zhukov et al. Bound state properties of Borromean halo nuclei: 6He and 11Li. *Physics Reports* **231**.4 (1993), 151–199.

[5] Jim.belk. *Borromean Rings Illusion*. 2010. URL: `https://commons.wikimedia.org/wiki/File:Borromean_Rings_Illusion.png`.

[6] G Hagen et al. Charge, neutron, and weak size of the atomic nucleus. *Physical Review C* 2 (2015), 186–190. arXiv: `1509.07169v1 [nucl-th]`.

[7] H Hergert et al. The In-Medium Similarity Renormalization Group: A novel ab initio method for nuclei. *Physics reports* **621** (2016), 165–222.

[8] Jouni Suhonen. *From nucleons to nucleus*. Springer, 2007.

[9] Willem H Dickhoff and Dimitri Van Neck. *Many-body Theory Exposed!: Propagator Description Of Quantum Mechanics In Many-body Systems*. Singapore: World Scientific, 2005.

[10] L. Trlifaj. Simple Formula for the General Oscillator Brackets. *Physical Review C* **5** (1972), 1534–1539.

[11] D.H. Gloeckner and R.D. Lawson. Spurious center-of-mass motion. *Physics Letters B* **53**.4 (1974), 313–318.

[12] R. Machleidt and D.R. Entem. Chiral effective field theory and nuclear forces. *Physics Reports* **503**.1 (2011), 1–75.

[13] A. Ekström et al. Optimized Chiral Nucleon-Nucleon Interaction at Next-to-Next-to-Leading Order. *Physical Review Letters* **110** (19 2013), 192502.

[14] M. Kortelainen et al. Nuclear energy density optimization: Shell structure. *Physical Review C* **89** (5 2014), 054314.

[15] S. K. Bogner, R. J. Furnstahl, and R. J. Perry. Similarity renormalization group for nucleon-nucleon interactions. *Physical Review C* **75** (6 2007), 061001.

[16] Jane K. Cullum and Ralph A. Willoughby. *Lanczos Algorithms for Large Symmetric Eigenvalue Computations, Vol. 1*. Philadelphia, PA, USA: Society for Industrial and Applied Mathematics, 2002.

[17] Louis Komzsik. *The Lanczos Method: Evolution and Application*. Software, Environments and Tools. Society for Industrial and Applied Mathematics, 2003.

[18] R. J. Furnstahl, G. Hagen, and T. Papenbrock. Corrections to nuclear energies and radii in finite oscillator spaces. *Physical Review C* **86** (3 2012), 031301.

[19] S. A. Coon et al. Convergence properties of *ab initio* calculations of light nuclei in a harmonic oscillator basis. *Physical Review C* **86** (5 2012), 054002.

[20] C. Forssén et al. Converging sequences in the *ab initio* no-core shell model. *Phys. Rev. C* **77** (2 2008), 024301.

[21] P Maris, J P Vary, and A M Shirokov. Ab initio no-core full configuration calculations of light nuclei. *Physical Review C* **79**.1 (2009), 014308.

[22] SN More et al. Universal properties of infrared oscillator basis extrapolations. *Physical Review C* **87**.4 (2013), 044326.

[23] S. N. More et al. Universal properties of infrared oscillator basis extrapolations. *Physical Review C* **87** (4 2013), 044326.

[24] R J Furnstahl, S N More, and T Papenbrock. Systematic expansion for infrared oscillator basis extrapolations. *Physical Review C* **89**.4 (2014).

[25] RJ Furnstahl et al. Infrared extrapolations for atomic nuclei. *Journal of Physics G: Nuclear and Particle Physics* **42**.3 (2015), 034032.

[26] S König et al. Ultraviolet extrapolations in finite oscillator bases. *Physical Review C* **90**.6 (2014), 064007.

[27] David Djajaputra and Bernard R Cooper. Hydrogen atom in a spherical well: linear approximation. *European Journal of Physics* **21**.3 (2000), 261–267.

[28] Matthew Newville et al. *LMFIT: Non-Linear Least-Square Minimization and Curve-Fitting for Python*. 2014.

[29] B.A. Craig, D.S. Moore, and G.P. McCabe. *Introduction to the Practice of Statistics*. Macmillan Higher Education, 2010.

[30] Jun John Sakurai and Jim Napolitano. *Modern quantum mechanics*. Addison-Wesley, 2011.

[31] G Papadimitriou et al. Charge radii and neutron correlations in helium halo nuclei. *Physical Review C* **84**.5 (2011).

[32] Daniel Sääf. "Three-body systems in the no-core shell model". Lic. Thesis. Chalmers University of Technology, 2014.

[33] Petr Navrátil. Cluster form factor calculation in the *ab initio* no-core shell model. *Physical Review C* **70** (5 2004), 054324.

[34] L. Trlifaj. New relations for the general oscillator brackets. *Czechoslovak Journal of Physics* **24** (1974), 471–481.

[35] I. Brida and F.M. Nunes. Two-neutron overlap functions for 6He from a microscopic structure model. *Nuclear Physics A* **847**.1–2 (2010), 1–23.

[36] R Roth. "Private Communication". 2012.

[37] J.M. Bang et al. One- and two-nucleon overlap functions in nuclear physics. *Physics Reports* **125**.6 (1985), 253–399.

[38] M Fabre de la Ripelle. The potential harmonic expansion method. *Annals of Physics* **147**.2 (1983).

[39] N. K. Timofeyuk. Normalization of the (^{6}He,^{4}He) cross sections in the distorted-wave Born approximation. *Physical Review C* **63**.5, 054609 (2001), 054609.

[40] P Navrátil. Local three-nucleon interaction from chiral effective field theory. *Few-Body Systems* **41**.3-4 (2007), 117–140.